

# REPORT DOCUMENTATION PAGE

Public reporting burden for this collection of information is estimated to average 1 hour per response, including the time for reviewing instructions, searching existing data sources, gathering and maintaining the data needed, and completing and reviewing this collection of information. Send comments regarding this burden estimate or any other aspect of this collection of information, including suggestions for reducing this burden, to Washington Headquarters Services, Directorate for Information Operations and Reports (0704-0188), Washington, DC 20540-6001. Respondents should be aware that notwithstanding any other provision of law, no person shall be subject to a penalty for failing to comply with a collection of information if it does not have a valid OMB control number. PLEASE DO NOT RETURN YOUR FORM TO THE ABOVE ADDRESS.

AFRL-SR-AR-TR-03-

0425

1. REPORT DATE (DD-MM-YYYY)  
23-09-2003

2. REPORT TYPE  
Final

3. DATES COVERED (From - To)  
Jan 2001 - Jun 2003

4. TITLE AND SUBTITLE  
Optimal Design of Smart Structures

5a. CONTRACT NUMBER

5b. GRANT NUMBER  
F49620-01-1-0152

5c. PROGRAM ELEMENT NUMBER

5d. PROJECT NUMBER

5e. TASK NUMBER

5f. WORK UNIT NUMBER

6. AUTHOR(S)  
Gordon Parker, Bernhard Bettig, Wei Chen and Markus Buehler

7. PERFORMING ORGANIZATION NAME(S) AND ADDRESS(ES)

Michigan Technological Univ.  
1400 Townsend Dr.  
Houghton, MI 49931

8. PERFORMING ORGANIZATION REPORT  
NUMBER

20031028 175

9. SPONSORING / MONITORING AGENCY NAME(S) AND ADDRESS(ES)

USAF/AFRL  
AFOSR  
801 N. Randolph Street  
Arlington, VA 22203

10. SPONSORING / MONITORING AGENCY REPORT  
NUMBER

11. SPONSOR/MONITOR'S REPORT  
NUMBER(S)

12. DISTRIBUTION / AVAILABILITY STATEMENT

Distribution Statement A. Approved for public release; distribution is unlimited.

13. SUPPLEMENTARY NOTES

14. ABSTRACT

The goal of this study was to investigate the benefits of simultaneously designing an active structure's topology, active material treatment, and control law. Both static and dynamic structures were considered. The goal for static structure design was to satisfy given load capability and displacements when activated. The goal of the dynamic structure design was increased stability margin. It was found that simultaneous design increases the performance as compared to a conventionally designed structure. The topology of the structure and the active material treatment work together to create a system that is less sensitive to spillover instability. A library of homogeneous, mixed material finite elements were created to facilitate simultaneous topological optimization of active and conventional material structures. Additionally, a general, parallel processing active structure design tool was created that combines a genetic algorithm optimization code with commercially available finite element (ABAQUS) and control design (MATLAB) codes.

15. SUBJECT TERMS

Optimal design, active structures, smart structures, genetic algorithm

16. SECURITY CLASSIFICATION OF:

a. REPORT  
U

b. ABSTRACT  
U

c. THIS PAGE  
U

17. LIMITATION  
OF ABSTRACT

UU

18. NUMBER  
OF PAGES

53

19a. NAME OF RESPONSIBLE PERSON  
Gordon Parker

19b. TELEPHONE NUMBER (include area  
code)  
(906) 487-1850

SEP 26 2003

Dr. Dean Mook  
Program Manager  
AFOSR  
801 N. Randolph Street  
Arlington, VA 22203

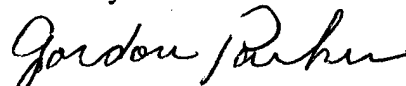
September 24, 2003

Re: Final Report: Optimal Design of Smart Structures

Dear Dr. Mook:

Enclosed please find a copy of the final technical report for "Optimal Design of Smart Structures," under grant number F49620-01-1-0152. Please let me know if I can submit the additional copies to DTIC.

Sincerely



Gordon Parker  
Associate Professor  
[ggparker@mtu.edu](mailto:ggparker@mtu.edu)

Final Technical Report:  
Optimal Design of Smart Structures  
F49620-01-1-0152

Gordon Parker (PI)  
Bernhard Bettig (Co-PI)  
Wei Chen  
Markus Buehler

Michigan Technological University  
815 R.L. Smith  
1400 Townsend Drive  
Houghton, MI 49931

September 23, 2003

Dr. Dean Mook  
AFOSR Program Manager

Sponsored by:  
Air Force Office of Scientific Research,  
Air Force Materiel Command, USAF, under grant number F49620-01-1-0152.

*The views and conclusions contained herein are those of the authors and should not be interpreted as necessarily representing the official policies or endorsements, either expressed or implied, of the Air Force Office of Scientific Research or the U.S. Government.*  
*Approved for public release; distribution is unlimited.*

<b>CONTENTS</b>	<b>1</b>
<b>Contents</b>	
<b>List of Figures</b>	<b>2</b>
<b>List of Tables</b>	<b>4</b>
<b>1 Foreward</b>	<b>5</b>
<b>2 Objective</b>	<b>6</b>
<b>3 Personnel Supported</b>	<b>7</b>
3.1 Principal Investigators . . . . .	7
3.2 Other Personnel . . . . .	7
<b>4 Executive Summary</b>	<b>8</b>
<b>5 Accomplishments</b>	<b>10</b>
5.1 The Active Material Extended Unit Cell . . . . .	10
5.1.1 Homogenization of the extended unit cell . . . . .	10
5.1.2 Design of a Structure and Embedded Actuator with Maximum Activated Deflection . . . . .	15
5.1.3 Solution of Optimization Problem . . . . .	18
5.1.4 Results . . . . .	18
5.1.5 Discussion . . . . .	21
5.2 Parallel Genetic Algorithm Active Structure Design Code . . . . .	23
5.3 Simultaneous Optimal Design of an Active Structure . . . . .	27
5.3.1 Simultaneous Optimization of the Sensors and Controller . . . . .	27
5.3.2 Simultaneous Optimization of an Active Structure . . . . .	40
<b>6 Publications</b>	<b>47</b>
6.1 Peer-Reviewed Publications . . . . .	47
6.2 Publications in Conference Proceedings . . . . .	47
6.3 Theses . . . . .	47
<b>7 Interactions and Transitions</b>	<b>48</b>
<b>8 New Discoveries, Inventions, and Patent Disclosures</b>	<b>49</b>
<b>9 Honors and Awards</b>	<b>50</b>

## List of Figures

1	Generic design case in topology optimization. . . . .	11
2	Illustration of the homogenization process. . . . .	11
3	Unit cells (a) classical (b) new extended unit cell. . . . .	13
4	The effective elastic coefficients $c_{ijkl}^h$ as a function of $a^2$ and $b^2$ . . . . .	14
5	The effective piezoelectric stress coefficient $e_{122}^h = e_{211}^h$ and effective permittivity coefficients $\epsilon_{11}^h = \epsilon_{22}^h$ as a function of $a^2$ and $b^2$ . . . . .	15
6	Design case for maximizing the tip deflection with the virtual force for the structural stiffness criterion. . . . .	16
7	Optimized designs for two sets of volume constraints. Conventional material is shown black and active material is shown grey. From left to right: (a,f) raw optimization results, (b,g) interpretation of the results, (c,h) deflection with force applied and electrical power switched off, (d,i) negation of deflection when electrical power is switched on, (e,j) possible "continuous" interpretation. . . . .	19
8	Topology optimization of a clamp mechanism: systematically changing the volume constraints, as well as changing the shape of the design domain from rectangular (1) to square (2). . . . .	20
9	Varying the strength of the virtual force. Gray structure shows the results when only the electric field is applied. Dark (color) structure shows the results when a force of constant magnitude is applied. Graph shows the tip deflection with and without the force applied, as a function of the virtual force. . . . .	21
10	Development of the objective function (a) and the constraint error (b) over the iterations, for the three different optimization cases shown in Figure 9. . . . .	22
11	Flow of the genetic algorithm based active structure design code. Green blocks indicate where fitness function calculations are required and are shown in detail in Figure 12 . . . . .	25
12	Flow of the evaluation of a member's fitness using an integration of ABAQUS and Matlab® . . . . .	26
13	Side and top views of the pinned-pinned beam with the two different sensor design domains configurations considered in the design example. . . . .	29
14	Unit cell defining the microstructure . . . . .	30
15	Homogeneous $e_{31}$ as a function of density $\rho$ for a microstructure . . . . .	31
16	The optimal normalized PVDF density as a function of beam position for both sensor configurations. In both cases the PVDF was optimized using the observability gramian cost function $\mathcal{J}_1$ . . . . .	35
17	The optimal normalized PVDF density as a function of beam position for both sensor configurations. In both cases the PVDF was optimized using the LQR stability margin cost function $\mathcal{J}_2$ . . . . .	36
18	Pole locations with uniform density distributions. Mode numbers are given for select mode shapes. . . . .	37
19	The approximate optimal normalized PVDF density for both sensor configurations. . . . .	38
20	Cantilever beam model. . . . .	41
21	Control block diagram. . . . .	42

22	Pole locations of the system with initial density setup. . . . .	43
23	Simulation and Experiment sensor signals of the open loop system. . . . .	44
24	Optimal distributions for conventional beam, PZT actuator and PVDF sensor. . . . .	45
25	Simulated sensor signals of the optimal, closed-loop system. . . . .	46

## List of Tables

1	Physical parameters of the pinned-pinned beam of the example. . . . .	28
2	Cost Function Values of Optimal Distribution of Discrete PVDF . . . . .	34
3	Cost Function Values of Optimal Distribution of Segmented Distributed PVDF	34
4	Comparison of observability gramian values for both sensor domains ('Disc' = Discrete, 'Seg. Dist' = Segmented Distributed). In addition to the nominal distributions, both the $\mathcal{J}_1$ and $\mathcal{J}_2$ optimal distributions are shown. . . . .	39
5	Physical parameters of the cantilever beam of the example. . . . .	41

## 1 Foreward

This report summarizes the research performed for the Air Force Office of Scientific Research under Contract No. FA9620-01-1-0152, "Optimal Design of Smart Structures." The contract began on January 1, 2001 and ran through June 30, 2003. The Principal Investigator was Professor Gordon G. Parker, Department of Mechanical Engineering - Engineering Mechanics at Michigan Technological University. The co-PI was Professor Bernhard Bettig, also of Michigan Technological University. The AFOSR program manager was originally Dr. Daniel Segalman with Dr. Dean Mook taking over in 2002.



## 2 Objective

The objective of this two-year research was to develop a methodology and the required analysis tools for simultaneous optimization of active structures considering:

- the conventional structure topology
- the active material layout
- the control system

This is in contrast to the typical active structure design approach of applying an active material treatment to an *existing* structure. Our hypothesis was that if the high level design goals were defined (e.g. stiffness, static deflection when active, closed-loop damping characteristics, etc.) without specifying the topology of the structure, nor the active material treatment and controller, then a better final design could be achieved by designing these features simultaneously making the structure and the controller work harmoniously.

### 3 Personnel Supported

This research was conducted primarily by the faculty and graduate students at Michigan Technological University as described below.

#### 3.1 Principal Investigators

Gordon G. Parker, Associate Professor of Mechanical Engineering, Michigan Technological University, 815 R.L. Smith Building, 1400 Townsend Drive, Houghton, MI 49931, Tel: (906) 487-1850, Fax (906) 487-2822, email: ggpark@mtu.edu.

Bernhard Bettig, Assistant Professor of Mechanical Engineering, Michigan Technological University, 815 R.L. Smith Building, 1400 Townsend Drive, Houghton, MI 49931, Tel: (906) 487-1897, Fax (906) 487-2822, email: bettig@mtu.edu.

#### 3.2 Other Personnel

This section contains a list of graduate students who received support from this project.

Markus J. Buehler, M.S. 2001, "Homogenization of Smart Material Cells for Topological Optimization." Current contact information: M.S. Research Assistant, Max-Planck-Institut für Metallforschung, Heisenbergstrasse 3, 70569 Stuttgart, Tel: ++49-(0)711-689-3579, Fax: ++49-(0)711-689-3512, email: m.buehler@mf.mpg.de.

Wei Chen, Ph.D. Candidate, "Optimal Design of Active Structures," Michigan Technological University, 815 R.L. Smith Building, 1400 Townsend Drive, Houghton, MI 49931, Tel: (906) 487-2271, Fax (906) 487-2822, email: wechen@mtu.edu.

Charles Kiilunen, Ph.D. Student, "Parallel Structural Design Optimization," Michigan Technological University, 815 R.L. Smith Building, 1400 Townsend Drive, Houghton, MI 49931, Tel: (906) 487-2271, Fax (906) 487-2822, email: cpkiilun@mtu.edu.

## 4 Executive Summary

The primary objective of this work was to explore the hypothesis that simultaneous design of an active structure's topology, active material treatment, and controller should yield better performance than designing an active material treatment for an existing structure, followed by the control design. Instead of tackling this problem in its entirety from the onset, a step-wise approach was used. Specifically, the active structural design problem was considered first for static deflection and force requirement satisfaction. This required the development of new unit cells, comprised of both conventional and active material, for finite element based topological optimization. After demonstrating this capability with several examples, it was extended to dynamic analysis. The example considered was the optimal design of an active beam where both the beam and the active material topology were optimized simultaneously. This problem was also decomposed into simpler subproblems for initial exploration, specifically

1. simultaneous structure, sensor, and controller design
2. simultaneous structure, sensor, actuator and controller design

During this process insight was gained not only on cost function selection, but also on how to formulate the control design portion of the problem. The main conclusions and achievements were

- development of a library of finite element cells with varying density of active and conventional material for use in spatial topological optimization
- development of a virtual force approach for specifying structural strength requirements during the optimal design process
- simultaneous optimal design can be used to decrease controller spillover effects, thus, increasing system performance
- topological optimization of both the conventional and active material can be used to generate realizable designs
- the shape of an active structure is dominated by the shapes of the modes that cause spillover instability when the design goal is increased stability margin

Several unexpected challenges arose during the project, leading to additional interesting and useful results. For example, to test an optimal active beam design a shaped piezoceramic laminate actuator was needed. Machining methods were investigated and it was found that a water jet approach was suitable for cutting, without fracturing, the ceramic actuator.

One of the most important aspects of this project was the development of an optimal design code for active structures. Although the development of such a general code was not an intention of the original project, it seemed to be the most logical approach as the project developed. The code uses a parallel (cluster-based) genetic algorithm written during the project. Parallelization was deemed necessary due to the potentially large optimization problems that could be encountered in the future. It supports any user-defined cost function

and constraints. However, since it was designed for structural optimization, it was linked to ABAQUS for general finite element calculations and Matlab® for rapid control design. Using these off-the-shelf, general analysis codes, a wide range of practical active structure problems can be solved where the system's overall design, active material treatment and controller are designed together for maximum performance.

## 5 Accomplishments

In the remainder of this report the primary accomplishments are documented. Specifically, separate sections are dedicated to

- Development of a new topological optimization unit cell that includes both conventional and active material
- An overview of the optimal design code that combines a parallel GA with ABAQUS (for finite element analysis) and Matlab<sup>®</sup> (for control design).
- Simultaneous optimal design of an active structure

### 5.1 The Active Material Extended Unit Cell

Mechanical structures are designed to meet specific loading requirements. Typically the designs are iterated “by hand”, changing design features and dimensions again and again until a reasonable result is obtained. The question of whether a chosen structure is optimal arises often. Topology optimization, first developed by Bendsoe and Kikuchi (1988) [12], automates the process of finding an optimal structural design. For a given set of boundary conditions and design specifications (constraints), a topology is computed that is optimal in terms of a formulated cost function. A generic design case is shown in Figure 1 illustrating several boundary and loading conditions. A typical objective function is minimization of structural compliance and a typical constraint is limiting the total volume of structural material to a percentage of the design domain volume. Bendsoe and Kikuchi defined the optimal structure as the optimal distribution of material [12]. To obtain different densities of constituent material at each point of the design domain, a parametrically defined microstructure with a variable size hole was introduced. A homogenization technique was used to obtain the effective elastic properties for a material having an infinitely fine occurrence of the microstructure [3, 18, 4, 10]. To solve for the optimal topology the design domain was discretized into a grid of finite elements. Since each finite element was defined parametrically, and could vary in density from 0 (no material) to 1 (solid material), the topology optimization problem could be transformed into a parameter optimization problem.

This section documents the development of a new extended unit cell that permits the simultaneous design of the structure and its active material treatment. An example is provided for a mechanism that changes shape when an electric field is applied while achieving specified loading requirements.

#### 5.1.1 Homogenization of the extended unit cell

In order to perform the topological optimization, it is necessary to know the structural properties of the unit cell as a function of the density parameters which are selected during optimization. Using underlying, microscopic structures to obtain these properties, as is done with homogenization, results in topology optimization problems that have proven to be well-converging [3, 22]. Compared to Simple Isotropic Material with Penalization (SIMP) approaches for obtaining structural properties, homogenization has numerical as well as physical advantages.

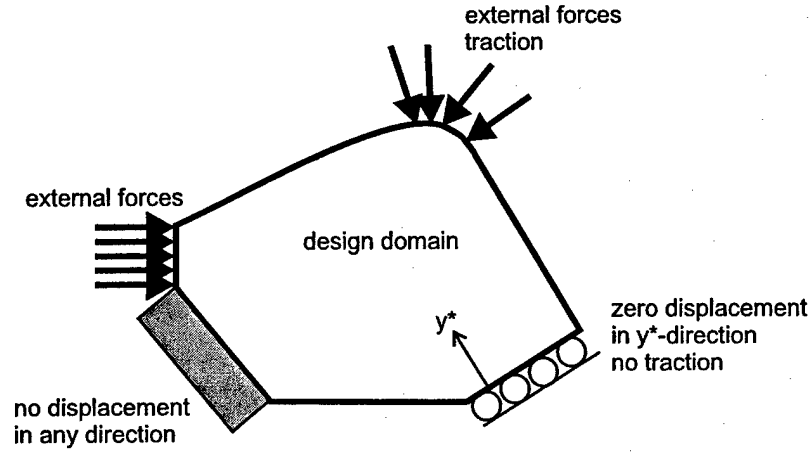


FIGURE 1: Generic design case in topology optimization.

Homogenization is a limit taking process as illustrated in Figure 2, where a first order asymptotic expansion is used to find effective material properties [3, 4, 24, 6]. Silva et al. (1999)[24] gives a complete description of the numerical homogenization of single material cells. A brief review is given here for the purpose of introducing the novel extended unit cell in the next section.

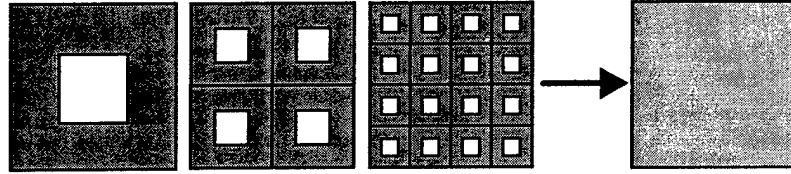


FIGURE 2: Illustration of the homogenization process.

The constitutive electromechanical equations of a piezoceramic material are:

$$\begin{aligned}\sigma_{ij} &= c_{ijkl}\epsilon_{kl} - e_{kij}E_k, \\ D_i &= e_{ikl}\epsilon_{kl} + \epsilon_{ik}E_k.\end{aligned}\tag{1}$$

where the variables  $ijkl$  take on values 1, 2, 3 (1, 2 in two dimensional problems). The index values can also be thought of as coordinates  $x$ ,  $y$  and  $z$  ( $x \equiv 1$ ,  $y \equiv 2$  and  $z \equiv 3$ ), where  $\epsilon_{kl}$  is the strain tensor and  $\sigma_{ij}$  is the stress tensor. The elastic tensor is denoted by  $c_{ijkl}$ . Furthermore,  $E_k$  is the electric field and the electric displacement is denoted as  $D_i$ , while  $\epsilon_{ik}$  denotes the dielectric tensor and  $e_{kij}$  is the piezoelectric stress tensor.

Next, the strains of equation (1) are expressed using the typical strain-displacement equations

$$\epsilon_{ij} = \frac{1}{2} \left( \frac{\partial u_i}{\partial x_j} + \frac{\partial u_j}{\partial x_i} \right),\tag{2}$$

where material displacements are denoted as  $u_i$  in the spatial directions  $x_i$ . Similarly, the electric field is expressed in terms of the electric field potential  $\phi$  as

$$E_i = -\frac{\partial \phi}{\partial x_i}. \quad (3)$$

The differential form of the mechanical, dynamical and electrostatic equilibrium equations are given by

$$\begin{aligned} \frac{\partial \sigma_{ij}}{\partial x_j} + f_i &= 0, \\ \frac{\partial D_i}{\partial x_i} - q &= 0, \end{aligned} \quad (4)$$

where  $f_i$  are forces, and  $q$  the charge. The constitutive electromechanical equations are substituted into (4) yielding the weak form formulation.

To solve for homogenized material properties, displacements are expressed as the sum of micro- and macro-scale terms using an asymptotic expansion of the form  $u_i = u_i^0 + \epsilon u_i^1 + \dots$  and  $\phi = \phi^0 + \epsilon \phi^1 + \dots$  which are substituted into the weak form formulation. The size of the unit cell, denoted by  $\epsilon$ , is taken to zero in the limit while keeping the density constant. Following this, the microscopic problem is separated from the macroscopic problem yielding the following equations.

$$\begin{aligned} \int_Y \left( c_{ijkl} \frac{\partial \chi_k^{pq}}{\partial y_l} \frac{\partial v_i}{\partial y_j} + e_{kij} \frac{\partial \Gamma^{pq}}{\partial y_k} \frac{\partial v_i}{\partial y_j} \right) dY &= \int_Y c_{ijpq} \frac{\partial v_{1i}}{y_j} dY, \\ \int_Y \left( e_{ikl} \frac{\partial \alpha}{\partial y_i} \frac{\partial \chi_k^{pq}}{\partial y_l} - \epsilon_{ik} \frac{\partial \Gamma^{pq}}{\partial y_k} \frac{\partial \alpha}{\partial y_i} \right) dY &= \int_Y e_{ipq} \frac{\partial \alpha}{y_i} dY. \end{aligned} \quad (5)$$

$$\begin{aligned} \int_Y \left( c_{ijkl} \frac{\partial z_k^p}{\partial y_l} \frac{\partial v_i}{\partial y_j} + e_{kij} \frac{\partial Z^p}{\partial y_k} \frac{\partial v_i}{\partial y_j} \right) dY &= \int_Y e_{pij} \frac{\partial v_{1i}}{y_j} dY, \\ \int_Y \left( e_{ikl} \frac{\partial \alpha}{\partial y_i} \frac{\partial z_k^p}{\partial y_l} - \epsilon_{ik} \frac{\partial Z^p}{\partial y_k} \frac{\partial \alpha}{\partial y_i} \right) dY &= - \int_Y \epsilon_{ip} \frac{\partial \alpha}{y_i} dY. \end{aligned} \quad (6)$$

$$\forall v_i, \alpha \in H^1(Y),$$

In these equations,  $p$  and  $q$  take on the same set of values as  $i$  and  $j$  (depending on the dimensionality of the problem.) The domain of the unit cell is denoted by  $Y$ , while  $v_i$  and  $\alpha$  are test functions. The functions  $\chi_k^{pq}$ ,  $\Gamma^{pq}$ ,  $z_k^p$  and  $Z_k^p$  are characteristic displacements, which are calculated from the equations and are constrained to be periodic in  $Y$ . The calculated characteristic displacements are then used in the following integrations to calculate the effective, homogenized material properties.

$$c_{ijkl}^h = \frac{1}{|Y|} \int_Y \left( c_{ijkl} - c_{ijpq} \frac{\partial \chi_p^{kl}}{\partial y_q} - e_{pij} \frac{\partial \Gamma^{kl}}{\partial y_p} \right) dY \quad (7)$$

$$e_{kij}^h = \frac{1}{|Y|} \int_Y \left( e_{kij} - c_{ijpq} \frac{\partial z_p^k}{\partial y_q} - e_{pij} \frac{\partial Z^k}{\partial y_p} \right) dY \quad (8)$$

$$e_{ikl}^h = \frac{1}{|Y|} \int_Y \left( e_{ikl} + \epsilon_{ip} \frac{\partial \Gamma^{kl}}{\partial y_p} - e_{ipq} \frac{\partial \chi_p^{kl}}{\partial y_q} \right) dY \quad (9)$$

$$\epsilon_{ik}^h = \frac{1}{|Y|} \int_Y \left( \epsilon_{ik} - \epsilon_{ip} \frac{\partial Z^k}{\partial y_p} + e_{ipq} \frac{\partial z_p^k}{\partial y_q} \right) dY, \quad (10)$$

To address the active structure problem, a new unit cell was developed that features both conventional as well as active material. This extended unit cell is shown in Figure 14(b), while a classical unit cell featuring one material is shown in Figure 14(a). The parameters  $a$  and  $b$  can vary, so that any possible density of active material ( $\rho_s$ ), conventional material ( $\rho_c$ ) and void ( $\rho_v$ ) can be obtained, so long as the total volume of material and void stays constant ( $0 \leq a \leq b \leq 1$ ). The densities of the active and conventional materials are given by  $\rho_s = 1 - b^2$  and  $\rho_c = b^2 - a^2$  respectively. The fraction of void per unit area is denoted by  $\rho_v = a^2$ . This enables the optimal material distribution task to be formulated as a parameter optimization problem.

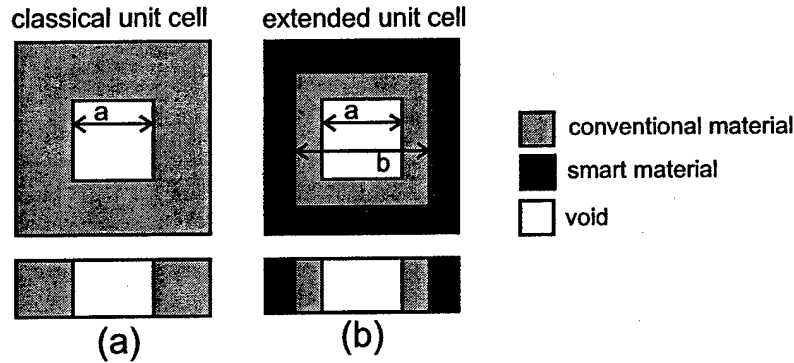


FIGURE 3: Unit cells (a) classical (b) new extended unit cell.

To use the homogenization results for topology optimization the homogenization equations of (7) are solved numerically for discrete values of  $a$  and  $b$ . For each combination of values, the characteristic displacements are first calculated using a Galerkin finite element method. The unit cell is discretized using quadrilateral, bilinear Lagrangian finite elements with incompatible nodes. The integrations are performed using Gaussian quadrature, and a sparse-matrix based inversion method is used to solve the resulting set of linear equations. The finite element formulation features two mechanical degrees of freedom, and one electrical degree of freedom per node. There are four nodes per finite element. Plane strain elements



are used, corresponding to a very thick plate. Further details regarding the implementation of the numerical method are available in Buehler *et al.* [6] and Bathe [2]. These discrete homogenization results are then used to perform a polynomial surface fit yielding an analytical function for each material coefficient. A 6th order polynomial was found to be sufficient.

Figures 4 and 5 show typical results. In this example, the piezoelectric material, by itself, has elasticity coefficients  $c_{iiii} = 2.1978 \times 10^7$ ,  $c_{1122} = 0.6593 \times 10^7$  and  $c_{1212} = 0.7692 \times 10^7$ . The piezoelectric stress coefficients are  $e_{211} = e_{122} = 0.1$  and the permittivity is  $\epsilon_{ii} = 1.140 \times 10^{-7}$ . The conventional material, by itself, has elasticity coefficients  $c_{iiii} = 1.12 \times 10^7$ ,  $c_{1122} = 0.323 \times 10^7$  and  $c_{1212} = 0.399 \times 10^7$ . Both materials are isotropic. The homogenized material elastic properties  $c_{ijkl}$  are plotted in Figure 4. The effective piezoelectric stress coefficient  $e_{122}^h = e_{211}^h$  and permittivities  $\epsilon_{11}^h = \epsilon_{22}^h$  as a function of the parameters  $a^2$  and  $b^2$  are shown in Figure 5, where all quantities are assumed to be unit-less. The behavior of the composite approaches the pure material when  $a = 1$  and  $b = 0$ , or vice versa. All material coefficients not shown are zero.

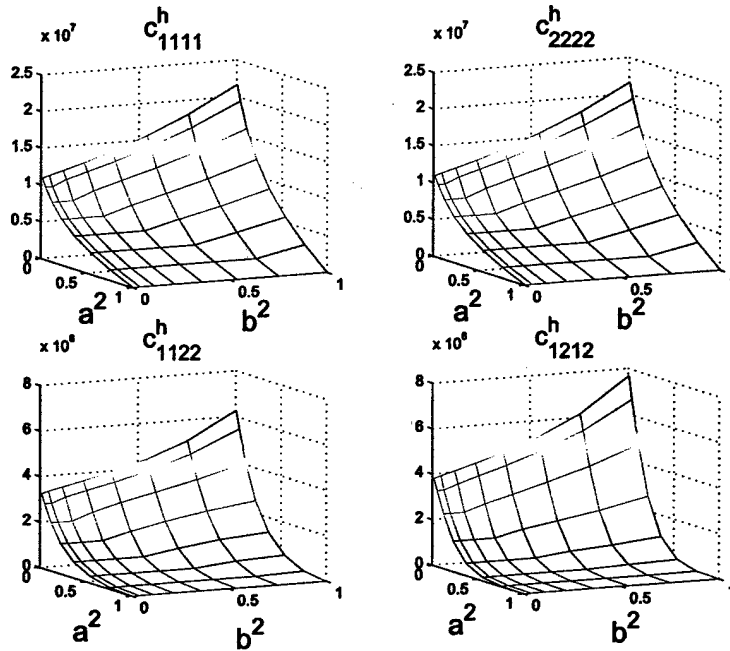


FIGURE 4: The effective elastic coefficients  $c_{ijkl}^h$  as a function of  $a^2$  and  $b^2$ .

The piezoelectric material we use is a "fictitious" isotropic piezoelectric material without a poling direction. In "classical", "real" active materials, there usually exists a poling direction, for example that determines in which orientation the material expands when an electrical field is applied. The concept of using this material model is motivated by the desire to have a material that expands in the  $y$  direction once an electrical field is applied in the  $x$  direction, and expands in the  $x$  direction once an electrical field is applied in the  $y$  direction. The expansion is always orthogonal to the electric field vector. Once the electric field vector is known, the model piezoelectric material can be replaced by real piezoelectric material which has the poling direction according to the electric field vector.

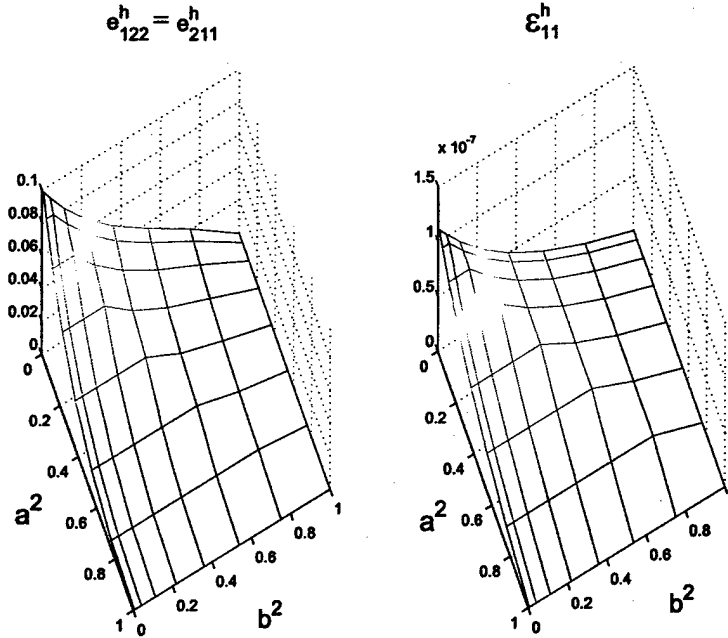


FIGURE 5: The effective piezoelectric stress coefficient  $e_{122}^h = e_{211}^h$  and effective permittivity coefficients  $\epsilon_{11}^h = \epsilon_{22}^h$  as a function of  $a^2$  and  $b^2$ .

In the discretization of the design domain into finite elements, a different microstructure is admitted in each element leading to different densities in each element. The whole set of design parameters is denoted by  $\mathbf{a} = (a, b)$ . The expression of material properties as a function of  $(a, b)$  makes it possible to treat the microstructure by effective material properties, instead of modeling the microstructure completely.

### 5.1.2 Design of a Structure and Embedded Actuator with Maximum Activated Deflection

The goal is to synthesize a structure that converts electrical into mechanical energy where the cost function is defined by the displacement of a specific node. With this scheme, smart structures are designed that output a deflection at a defined location when electrical power is applied. In this example, the tip deflection of the lower left node, denoted  $(x_0, y_0)$ , as shown in Figure 6 is to be maximized. We assume that a constant electric field is applied in the design domain with a constant gradient of the electric potential in the direction shown. In addition to the pure displacement-based cost function, we introduce a stiffness criterion using an additional virtual boundary force  $F_v$  acting in the opposite direction of the desired displacement. The criterion does not appear in the cost function or the constraints directly, but is only present as a boundary condition when the finite element problem is solved.

Since the electric field is only in one direction, the “fictitious” material is only actuated in one direction, making it equivalent to an  $e_{31}$  material (actuated in the up and down direction). At this point, the electric field is just given without any consideration for how it can be realized. This is discussed later in the discussion section.

Usually, in compliant mechanism design, or piezoelectric actuator design, optimization

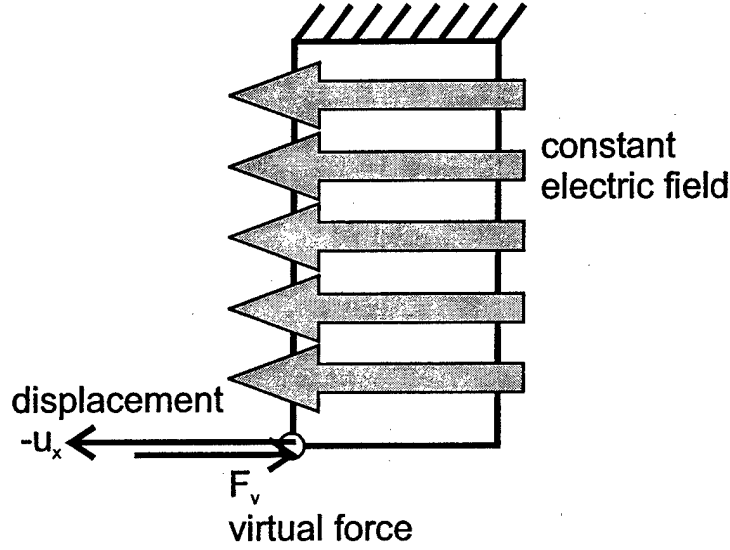


FIGURE 6: Design case for maximizing the tip deflection with the virtual force for the structural stiffness criterion.

of displacement of a given point is achieved by maximizing the mean mutual energy, or the mean transduction [19, 25, 21]. To provide stiffness, the mean compliance is minimized in both cases. In this example, we propose a somewhat different scheme to achieve the same goal, which is large displacement on the one hand, and sufficient stiffness of the structure on the other hand. Our approach of optimizing the deflection at a chosen point is related to the maximization of an equivalent mutual energy (or mean transduction). However, the stiffness criterion is achieved by applying a dummy load.

The stiffness criterion and the deflection criterion are essentially counteracting, and a tradeoff is required in the final solution. In very compliant structures, one can have large displacements, but no force. On the other hand, in very stiff structures, there is little displacement, but large forces. In the classical approaches, prior to optimization a parameter has to be chosen which determines the relative strength of the stiffness criterion versus the deflection criterion [19, 25, 21]. In the method illustrated in this example, the relative strength has to be chosen carefully to obtain useful designs, here by selecting the strength of the force versus the strength of the electric field.

The cost function is  $\mathcal{J}(\mathbf{a}) = -u_x(x_0, y_0)$ , capturing the  $x$  displacement of the lower left node. The displacements  $u_x$  are subject to the “constraints” of satisfying the equilibrium equations of (4). These are implemented by defining four symmetric bilinear operators (for details, see e.g. [16]):

$$\begin{aligned} a(u, v) &= \int_{\Omega} c_{ijkl} \frac{\partial u_k}{\partial x_l} \frac{\partial v_i}{\partial x_j} d\Omega, & b(\phi, v) &= \int_{\Omega} e_{ikl} \frac{\partial \phi}{\partial x_i} \frac{\partial v_k}{\partial x_l} d\Omega, \\ c(u, \alpha) &= \int_{\Omega} e_{kij} \frac{\partial u_i}{\partial x_j} \frac{\partial \alpha}{\partial x_k} d\Omega, & d(\phi, \alpha) &= \int_{\Omega} \epsilon_{ik} \frac{\partial \phi}{\partial x_i} \frac{\partial \alpha}{\partial x_k} d\Omega, \end{aligned} \quad (11)$$

where  $v_i$  and  $\alpha$  are test functions that satisfy the boundary conditions. Note that two

operators are equivalent  $c(u, \alpha) = b(\alpha, u)$ . The right hand sides of the piezoelectric equations of (4) are represented by four additional operators,

$$F_{m;\Gamma}(t, v) = \int_{\Gamma} t_i v_i d\Gamma, \quad (12)$$

$$F_{e;\Gamma}(q, \alpha) = \int_{\Gamma} q \alpha d\Gamma, \quad (13)$$

$$F_{m;\Omega}(F, v) = \int_{\Omega} F_i v_i d\Omega \quad (14)$$

$$F_{e;\Omega}(Q, \alpha) = \int_{\Omega} Q \alpha d\Omega, \quad (15)$$

where  $t_i$  are the traction forces,  $q$  are the applied charges at the boundaries,  $F$  and  $Q$  are the volumetric forces and charges respectively. This allows the piezoelectric equations to be expressed compactly as

$$\begin{aligned} a(u, v) + b(\phi, v) &= F_{m;\Gamma}(t, v) + F_{m;\Omega}(F, v), \\ c(u, \alpha) - d(\phi, \alpha) &= F_{e;\Gamma}(q, \alpha) + F_{e;\Omega}(Q, \alpha), \end{aligned} \quad (16)$$

$$\forall v_i, \alpha \in H^1(\Omega),$$

where  $\Omega$  refers to the design domain. The optimization problem can then be summarized as finding a set of elemental design parameters,  $a$  such that

$$\begin{aligned} \min_{a_i, b_i} : \mathcal{J}(a) &= -u_x, \\ \text{subject to : } a(u, v) + b(\phi, v) &= F_{m;\Gamma}(t, v) + F_{m;\Omega}(F, v), \\ c(u, \alpha) - d(\phi, \alpha) &= F_{e;\Gamma}(Q, \alpha) + F_{e;\Omega}(q, \alpha), \\ \forall v_i, \hat{\alpha} \in H^1(\Omega), \int_{\Omega} \rho_c d\Omega &= V_c V_0, \int_{\Omega} \rho_s d\Omega = V_s V_0, \\ 0 \leq a_i \leq 1, a_i \leq b_i &\leq 1. \end{aligned} \quad (17)$$

It should be noted that constraints are also imposed on the amount of material and on the elemental design parameters as described by equation (17). Specifically, volume constraints on active and conventional material are imposed, denoted by  $V_c$  and  $V_s$ , where  $V_0$  is the area of the design domain. In addition the design parameters are required to be continuous and between zero and unity.

### 5.1.3 Solution of Optimization Problem

Sequential Quadratic Programming (SQP) is used to solve the optimization problem of equation (17). At each iteration the cost function  $\mathcal{J}(\mathbf{a})$  is obtained using the finite element method. In the piezoelectric case, in addition to the stiffness matrix  $\mathbf{K}_{uu}$ , there are also the piezoelectric matrix  $\mathbf{K}_{u\phi}$ , as well as the dielectric matrix  $\mathbf{K}_{\phi\phi}$ .

The displacement of all nodes is in general given by  $\mathbf{u} = \mathbf{K}^{-1}\mathbf{F}$ , where  $\mathbf{K}$  is the assembled stiffness matrix,  $\mathbf{F}$  is the force vector, and  $\mathbf{u}$  is the displacement vector. It should be noted that both  $\mathbf{K}$  and  $\mathbf{F}$  depend on the design parameters  $\mathbf{a}$ . A constant electrical field is applied by specifying the electrical potential throughout the design domain. The elemental force vector is therefore given by  $\mathbf{F} = -\mathbf{K}_{u\phi}\boldsymbol{\phi}$ . In the present case for a constant electrical field in the  $y$  direction, the vector  $\boldsymbol{\phi} = [-\phi_0, 0, 0, -\phi_0]^T$  ( $\phi_0$  is related to the strength of the electric field, according to equation (3)). Therefore, the problem can essentially be solved as a conventional, completely elastic problem.

The cost function of (17) can be expressed using an additional mapping vector  $\mathbf{B}$ , that is,  $\mathcal{J}(\mathbf{a}) = \mathbf{B}(\boldsymbol{\Gamma})\mathbf{K}^{-1}(\mathbf{a})\mathbf{F}(\mathbf{a})$ . With this formulation any one displacement can be used as the cost function. Here, we simply need  $\mathbf{B} = [\mathbf{0} \dots \mathbf{0} \mathbf{1} \mathbf{0}]$ . Since the SQP method is gradient based, we also need the partial derivative of  $\mathcal{J}(\mathbf{a})$  with respect to the design parameters. This can be obtained directly, in the general form, from the finite element analysis results as

$$\frac{\partial \mathcal{J}(\mathbf{a})}{\partial \mathbf{a}} = -\mathbf{B}(\boldsymbol{\Gamma})\mathbf{K}^{-1}(\mathbf{a})\frac{\partial \mathbf{K}(\mathbf{a})}{\partial \mathbf{a}}\mathbf{K}^{-1}(\mathbf{a})\mathbf{F}(\mathbf{a}) + \mathbf{B}(\boldsymbol{\Gamma})\mathbf{K}^{-1}(\mathbf{a})\frac{\partial \mathbf{F}(\mathbf{a})}{\partial \mathbf{a}}. \quad (18)$$

We note that since the optimization problem is nonlinear, local minima can occur. A question is therefore whether the obtained solution is a local or a global minimum. To address this the optimization problem was solved for several different initial  $\mathbf{a}$  distributions. In each case, similar results were obtained providing confidence that the optimal distribution of smart and conventional material is close to a global minimum of the constrained objective function, however this is not intended to be proof of global optimality.

### 5.1.4 Results

In the first set of results a finite element discretization of  $40 \times 20$  was used in the topology optimization problems. The "raw", unprocessed optimization results for two discretizations in Figure 7(a) for an active material volume constraint of 20 percent, and a volume constraint of 30 percent for conventional material. In Figure 7(f) for an active material volume constraint of 30 percent, and a volume constraint of 40 percent for conventional material. Little checkerboarding is observed in both examples, and the smart and conventional material is well-separated.

It is often advantageous to post-process the data further. This is illustrated in Figure 7(b) and Figure 7(g). A finite element was considered comprised of completely active material if  $\rho_s > 0.50$ . Similarly, an element was considered comprised of completely conventional material when  $\rho_c > 0.50$ . Finite element analysis results are shown in Figure 7(c) and (h). An applied force leads to a deformation of the structure, as shown in Figure 7(c) and (h) with no field applied. The electric field is turned on in Figure 7(d) and (i) illustrating the negation of the force induced displacement. Figure 7(e) and (j) shows a possible interpretation of the

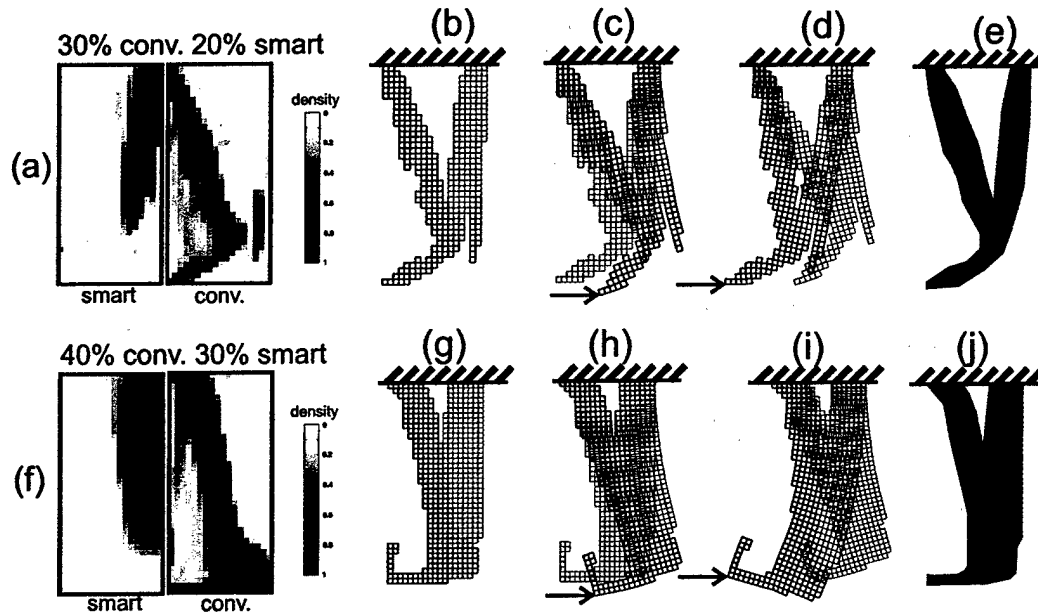


FIGURE 7: Optimized designs for two sets of volume constraints. Conventional material is shown black and active material is shown grey. From left to right: (a,f) raw optimization results, (b,g) interpretation of the results, (c,h) deflection with force applied and electrical power switched off, (d,i) negation of deflection when electrical power is switched on, (e,j) possible "continuous" interpretation.

resulting design using a contiguous segment of active material. An interesting observation is that it seems to put some of the conventional material in a place where it doesn't do anything (observe the vertical strip on the right in Figure 7 (a)-(d)). If this material were used on the left, likely it would make the structure stiffer, resulting in a smaller displacement when the structure is activated.

Another set of results of topology optimization of a clamp mechanism, systematically changing the volume constraint for the active material and the conventional material, as well as changing the shape of the design domain from rectangular (1) to square (2) is shown in Figure 8. In Figures 8(a)-(c), the active material constraint is kept constant at 30 percent, while the conventional material volume constraint varies from 8 to 30 percent. In Figures 8(c) and (e), the active material constraint is varied from 30 percent to 8 percent, while the volume constraint for active material is kept constant at 30 percent. The smart material tends to be put close to the fixed boundary. The optimization runs also reveal that the shape of the conventional material changes, when the amount of smart material is modified.

The resulting design is obviously affected directly by the volume constraints, however, the magnitude of the virtual force acting on the displaced node must also be chosen carefully. By changing the strength of the force, it is possible to affect the stiffness of the structure. Figure 9 (a) shows the resulting structures for different strengths of the virtual force. In this figure the gray colored shapes (deflecting to the left) show the structures with just the deflection due to the piezoelectric effect. The darker (colored) shapes show the structures with the piezoelectric effect and with the application of a constant force. In panels 1-4, the

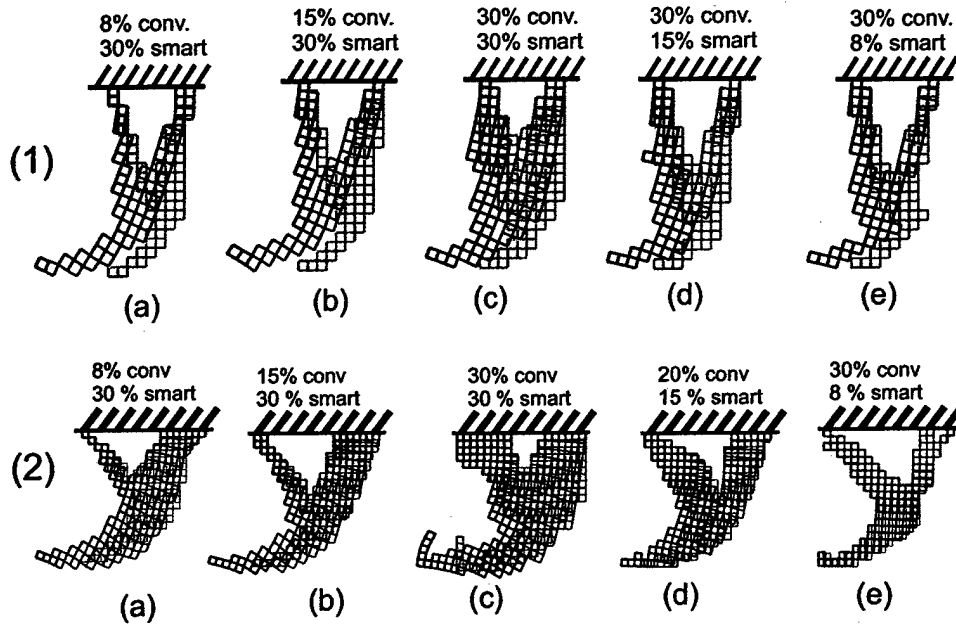


FIGURE 8: Topology optimization of a clamp mechanism: systematically changing the volume constraints, as well as changing the shape of the design domain from rectangular (1) to square (2).

virtual force is decreasing. It can be observed that if the force is small the displacement will be large when the PZT is activated, but the structure will be very compliant and will not be able to support even the small virtual force. It is also observed that if the virtual force is small, the structures often feature hinges. On the other hand, if the virtual force is large the structure will be stiff and the resulting displacements will be small, both with and without the virtual force. Figure 9 (b) shows the tip deflection with and without a force applied, as a function of the virtual force applied during the optimization.

The results in Figure 9 also indicate that there exists a convergence to an optimal solution once the virtual force is below or above a critical value (below 6,000 the resulting tip deflection does not change much, as for magnitudes of the virtual force above 11,000). Such behavior may be found in many design cases. However, there is no indication that the actual values would be identical in different problems. Therefore, it seems necessary that different values should be tried for a specific problem and then decided what is most suitable to achieve good results.

Finally, we discuss the convergence of the different problems studied in this work. Figure 10 (a) plots the development of the objective function over 76 iterations, for the four different optimization cases shown in Figure 9. It can be seen that the optimum solution is approached monotonically in each case.

In our calculations, the optimization is stopped when the material distribution is such that densities close to zero or one dominate in the design domain. This criterion could further be used to define a critical slope of the objective function with respect to iterations  $\Delta J$ . The optimization is then stopped once the change in cost becomes sufficiently small, e.g. below a threshold of  $\Delta J = 0.01$  between two iteration steps.

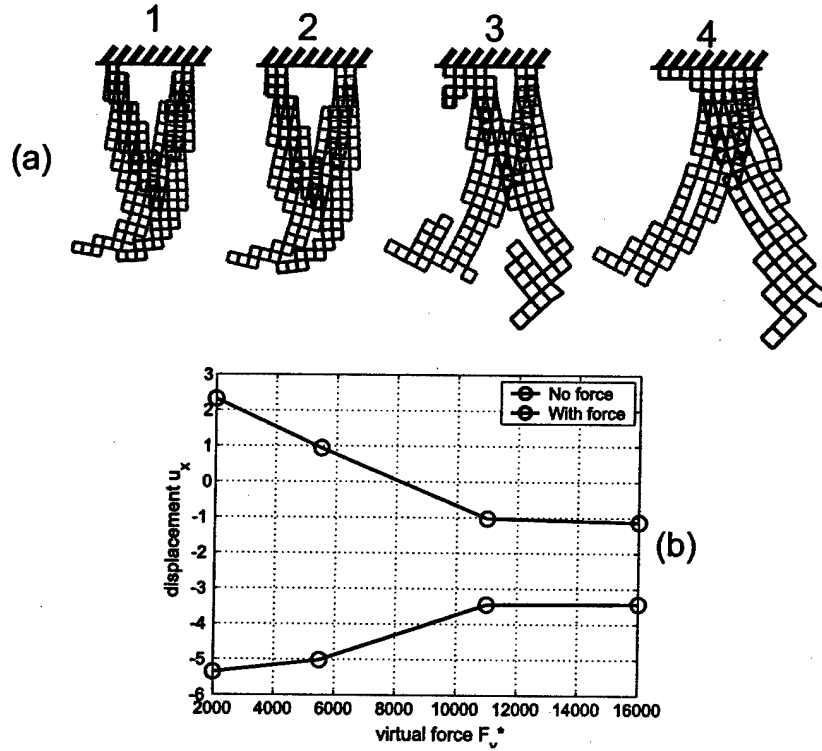


FIGURE 9: Varying the strength of the virtual force. Gray structure shows the results when only the electric field is applied. Dark (color) structure shows the results when a force of constant magnitude is applied. Graph shows the tip deflection with and without the force applied, as a function of the virtual force.

It is interesting to note that when a larger virtual force is used, the convergence is also faster (*cf.* cases 1 and 2 with large virtual force, and cases 3 and 4 with smaller virtual force).

Figure 10 (b) plots the constraint errors over the iterations for the four optimization cases shown in Figure 9. Figure 10 (b) proves that the constraints are always satisfied within an average deviation below  $1 \times 10^{-4}$ , at least for the cases 1-3 (when the virtual force gets very small as in case 4, convergence becomes poor). Convergence in the other cases considered (Figures 7 and 8) is very similar to the results shown in Figure 10 (a), case 1 and 2. Overall the optimizations typically required 60-80 iterations to converge while satisfying the constraints below an error of  $10^{-4}$ .

### 5.1.5 Discussion

The computations show that it is feasible to perform the numerical homogenization of a unit cell with parametrically defined densities of active material, conventional material, and void. They also show that it is feasible to use the resulting homogenized properties to perform a topological optimization in which there are no constraints on the position of the conventional or active material. As well, it was found that the different constituting materials are well-separated in the final solution.



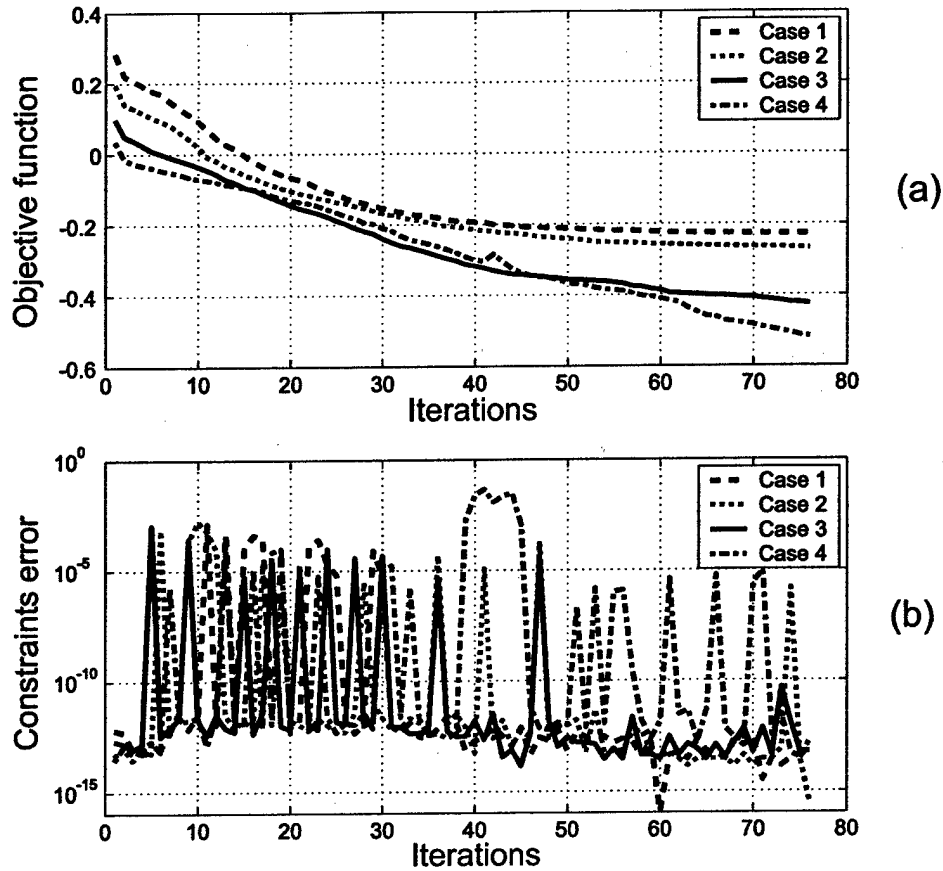


FIGURE 10: Development of the objective function (a) and the constraint error (b) over the iterations, for the three different optimization cases shown in Figure 9.

We find that it is crucial to include a stiffness criterion in order to obtain good designs, as clearly shown in Figure 9. This is in agreement with previous research on the topic [19, 25, 21]. Further discussion on the topic of competing design for compliance and stiffness for conventional structures could be found in a paper by Chen *et al.* (2001) [8].

It was observed that for very low volume fractions of both active and conventional material, the method is not as effective as in other cases. However, as can be seen in Figure 7(c), even for low volume fractions of active material good convergence is obtained.

The material we used in the examples is characterized by its piezoelectric coupling coefficients  $e_{211}$  and  $e_{122}$ , while all other piezoelectric stress coefficients were assumed to be zero. These piezoelectric properties were chosen in order to achieve a piezoelectric effect orthogonal to the applied electric field. Other choices (e.g.  $e_{111}$  and  $e_{222}$ ) are possible as well.

The principle aim of this research was not to synthesize structures that are manufacturable, but to develop general and basic principles. In terms of manufacturing the resulting structures, the proposed material microstructure is not literally acceptable. But, as the results show, regions with either one or the other material, or void, appear in the solution. As a result, manufacturing of a mixture of materials is not required.

The resulting topologies are also post-processed in order to interpret realizable structures that can be built. An interpretation using stack actuators is proposed which are added to the conventional structure in such a way that they have the desired effect. The electric field leads to an expansion (respectively contraction) in the orthogonal direction. Analyzing the resulting displacement, one can orient stack actuators (e.g. 3-3 piezoelectric material) properly and overcome the difficulty of having a 2-1 material with planar electric fields. Generally, if the active material covers the entire cross-section of a slender member such as the red area in Figure 7(e) and (j), then it may be possible to replace that with stack actuators. However, if only a part of the member cross section is made of active material, then under electric forces the member would be bending and it may not be possible to directly come up with a manufacturable part that will replace that member.

In some cases this allows building the resulting structures. For instance, the part in Figure 7(e) contains active material (red region) that could be realized by many stack layers. Using different sizes of these piezoelectric stack actuators, oriented in the proper orientation, even the optimal shape could be approximated. In this case, the electrodes would be oriented orthogonal to the direction of the active material beam portion of the topology optimization result.

## 5.2 Parallel Genetic Algorithm Active Structure Design Code

Both sequential quadratic programming (SQP) and genetic algorithm (GA) methods were used to solve the optimization problems in this project. Specifically, the `fmincon` function in Matlab®, an SQP code, was used to solve low dimensional optimization problems containing no more than 50 design parameters. This was the case for the static design example considered in Section 5.1 and for the optimal sensor design study that is described in Section 5.3.1. Although these problems were relatively small, it was found that running Matlab® on a single computer would be problematic for larger optimization problems and those requiring complex cost function evaluations.

Based on this realization it was decided that a general, parallel processing based approach should be developed. A genetic algorithm method was eventually selected since GAs can accommodate both discrete and continuous cost functions. A computing cluster formulation was chosen since these are more readily available to researchers and are scalable, as compared to single, multiprocessor computers.

**GA Code Description** The GA code was written in C using the Message Passing Interface (MPI) standard for sharing data between computers in the cluster. At a high-level, a GA code starts with an initial population consisting of  $N$  members. Members are defined by a genetic code that maps to discrete values of the design parameters. After initializing the population with randomly created members, all of their cost functions are computed and stored. New generations are created by cross-over and mutation, where the cost function of each new member must again be computed. When a new generation is created, the lowest cost function members are removed. This process continues for a fixed number of generations, or until some stopping criteria, for example based on the change of the member's net cost, is satisfied. A flow chart of the GA code developed during this project is shown in Figure 11.

At a lower-level, the parallel implementation allowed the available computers in the cluster to work on computing the cost functions for the members, thus reducing the time needed to evaluate a new generation. A 'master' computer was given the task of organizing how the members were distributed amongst the cluster. The GA code was written with sufficient generality to accomodate any number of computers in the cluster and was tested with up to 47 Sun workstations.

One important benefit of the GA approach over gradient based methods is that a set of near-optimal solutions is provided that may be in vastly different places in the design space. This provides the designer a set of different designs to choose from, facilitating the crucial capability of bringing human decision making into the optimization process. To implement this in a practical way, the capability was added to the code allowing a user to look at the best designs as the code is running. Additionally, the user can modify aspects of those designs, and re-insert them into the population. This real-time "seeding" capability is a unique feature of the design environment and is intended to bring together some of the best aspects of human-based design and computer-based design.

**Multidisciplinary Design Environment** There are three primary tasks for simultaneous active structure design

1. selection of parameter values that uniquely define the system consisting of both structural and control attributes
2. creation and analysis of the corresponding static or dynamic model defined by the structural parameters selected in step 1.
3. development of the control law based on the model created in step 2 and the control law parameters selected in step 1.

In the most general case it was expected that finite element analysis would be required so that mode shape and frequency information, a model of the structure, would be available for the control law design phase. For this purpose ABAQUS, a commercially available finite element code, was chosen. Similarly, to encompass the most general control law design possible, it was decided to facilitate the automatic inclusion of Matlab<sup>®</sup> into the optimal design code. Using low-level communication protocols within both ABAQUS and Matlab<sup>®</sup> it was eventually possible to create a fully integrated system where the GA generated the design parameters, passed the structural information to ABAQUS, along with the analysis instructions. The ABAQUS results were then automatically passed to Matlab<sup>®</sup>, along with control design instructions and the control related parameters from the GA. With the cost function evaluation definition originating from the GA, Matlab<sup>®</sup> could then design the controller and generate the cost function based on either time domain simulation or frequency domain analysis. A block diagram illustrating the process is shown in Figure 12.

This general framework was certainly sufficient for the active material systems considered in the examples of the following section. However, it has a broader range of applicability including automatic design of active truss systems, wing internal structures, etc. Other application areas are currently begin explored with Air Force agencies and DARPA.

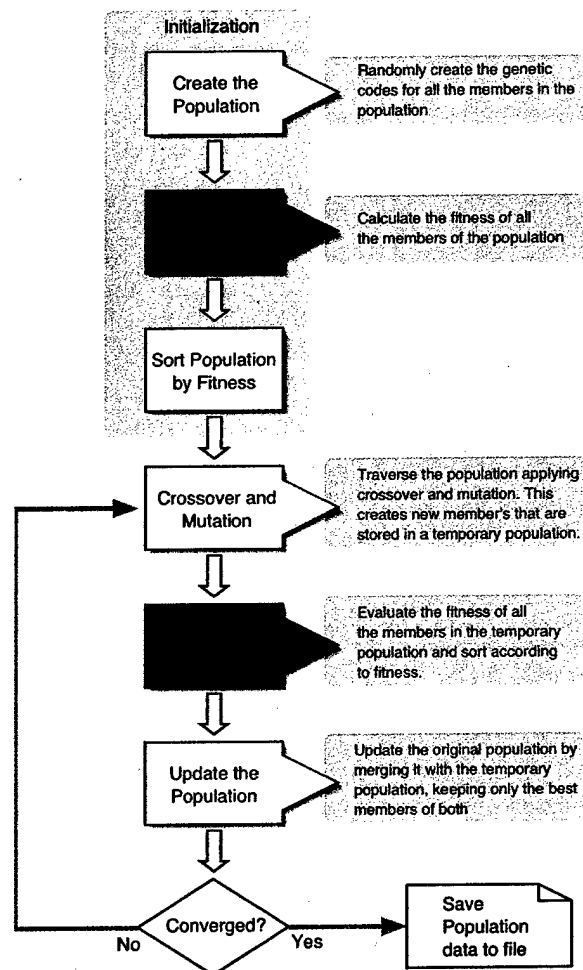


FIGURE 11: Flow of the genetic algorithm based active structure design code. Green blocks indicate where fitness function calculations are required and are shown in detail in Figure 12

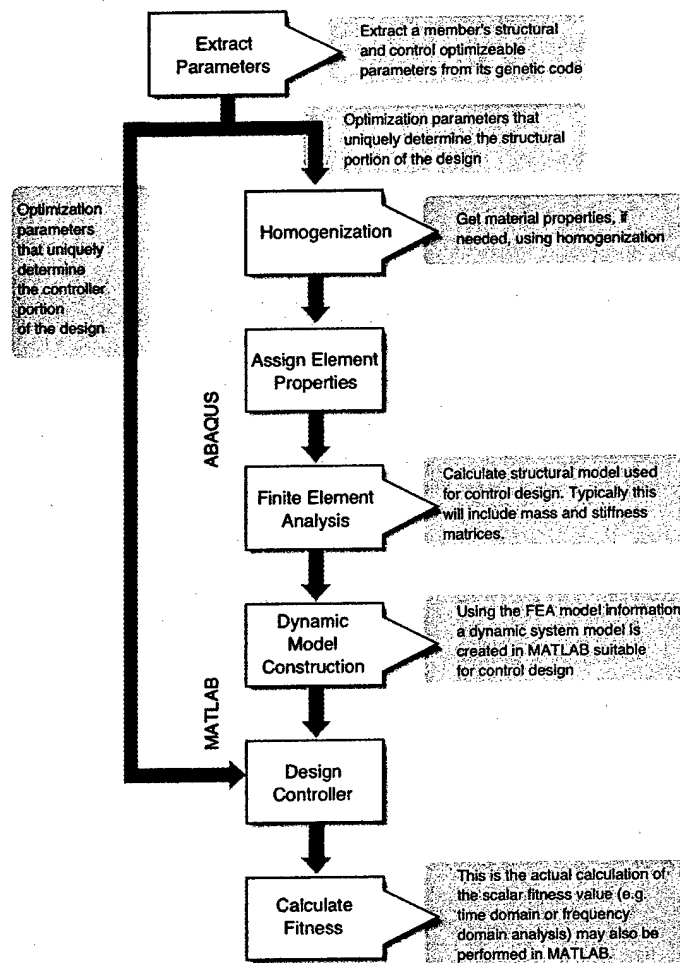


FIGURE 12: Flow of the evaluation of a member's fitness using an integration of ABAQUS and Matlab®

### 5.3 Simultaneous Optimal Design of an Active Structure

As described in the Executive Summary, an incremental approach was used leading up to full simultaneous design of a structure's conventional and active material as well as the controller. The results of these two steps are documented in the remainder of this section. First the simultaneous design of the sensor and controller package, given an existing structure is described. This exercise provided valuable insight into the cost function selection, and the approach for control design. Second the full simultaneous design problem is considered in Section 5.3.2.

#### 5.3.1 Simultaneous Optimization of the Sensors and Controller

Simultaneous optimization of the smart material distribution and the control strategy was investigated with the goal of improving the stability margin of a closed-loop active structure. This required extending the topological optimization for static structure requirements, described in section 5.1, to the dynamic case. In addition, investigation of suitable cost functions was performed. Through topological optimization of the active material sensor, using a homogenization approach and a linear quadratic regulator (LQR), a new type of sensor, with the ability to increase the closed-loop stability margin, was obtained.

One constraint that must be specified at the beginning of any topological optimization problem is the design domain size. In section 5.1 this was addressed in terms of volume fraction of active versus conventional material. In this section two different sensor design domains are considered (1) discrete (2) segmented distributed as shown in Figure 13. This type of comparison was performed to provide some insight into how the sensor design domain should be specified for a general structure. *The primary conclusion was that the segmented distributed domain provided better closed-loop performance, from a stability margin perspective.*

**Introduction** A controller that satisfies the design requirements for all admissible perturbations is termed robust[7]. As applied to the control of flexible structures, this means that a closed-loop controller must be able to operate in the presence of modelling uncertainties that lead to spillover instabilities. This has been studied extensively [1][15][17].

In this approach, a method for sensor design that increased the stability margin by simultaneously optimizing a Polyvinylidene Fluoride (PVDF) sensor distribution and the control strategy for a closed-loop system was developed. The approach was motivated by Collet[9] who illustrated optimal sensor design based on minimizing the observability gramian of the open loop system. Here a more general sensor design strategy was investigated which increased the range of the feedback gain directly. The specific case of decreasing the detrimental effect of sensing unmodelled modes is thus captured as a special case.

**Dynamic Model** The specific pinned-pinned beam system considered, along with the two sensor domains, is shown in Figure 13. A single point force actuator was postulated as the controlled input, located a distance  $L_a$  from one support.

The dynamic equation, relating external loads to beam vibration is

$$EI \frac{\partial^4 w(x, t)}{\partial x^4} + \rho A \frac{\partial^2 w(x, t)}{\partial t^2} = L(x)u(t) \quad (19)$$

where  $E$  is Young's modulus and  $I$  is the area moment of inertia of the steel beam,  $\rho$  is the mass density and  $A$  is its cross-sectional area, and  $L(x)$  is the position function of the actuator. The physical dimensions are given in Table 1.

Parameter	Units	Value
$L_a$	$m$	0.06
$L_b$	$m$	1.9
$L_{s1}$	$m$	0.19
$L_{s2}$	$m$	0.38
$w_b$	$m$	0.04
$t_b$	$m$	0.004
$\rho$	$kg/m^3$	7800
$E$	$N/m^2$	$210 \times 10^9$
$e_{31}^0$	$m/V$	$8.1987 \times 10^{-2}$

TABLE 1: Physical parameters of the pinned-pinned beam of the example.

An assumed modes solution takes the form

$$w(x, t) = \sum_{i=1}^n \eta_i(t) \phi_i(x) \quad (20)$$

where  $\eta_i(t)$  is the  $i$ th generalized coordinate and the pinned-pinned mode shapes  $\phi_i(x)$  are

$$\phi_i(x) = \sin(\beta_i x) \quad (21)$$

where the value of  $\beta_i$  can be determined from the frequency equation of the beam,  $\sin(\beta_i L_b) = 0$ .

In general, the equation of motion with damping can be written as

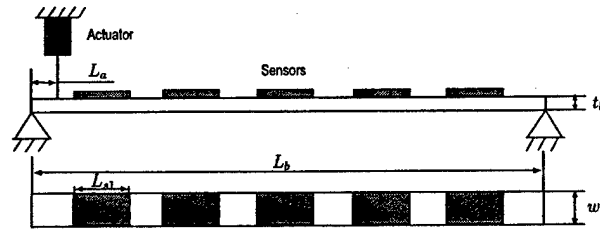
$$\ddot{\eta}_i(t) + 2\zeta\sqrt{\Lambda}\dot{\eta}_i(t) + \Lambda\eta_i(t) = B_i u(t) \quad (22)$$

where  $\zeta$  is the matrix with modal damping coefficients,  $\Lambda$  is the matrix of eigenvalues and the control weighting coefficient of the  $i$ th mode,  $B_i$ , is

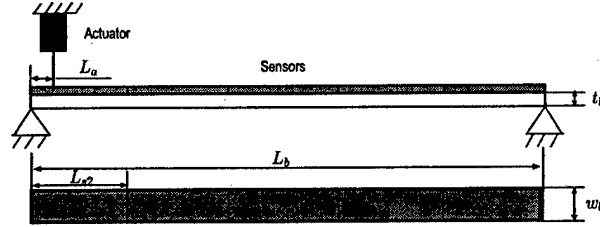
$$B_i = \int_{\Omega} \phi_i(x) L(x) d\Omega \quad (23)$$

where  $\Omega$  is the beam domain. The state space representation is

$$\begin{aligned} \dot{x} &= Ax + Bu \\ y &= Cx \end{aligned} \quad (24)$$



(A) Discrete PVDF sensors



(B) Segmented distributed PVDF sensors

FIGURE 13: Side and top views of the pinned-pinned beam with the two different sensor design domains configurations considered in the design example.

where the  $2n \times 1$  state vector  $x$  contains the generalized coordinates and their speeds, the  $2n \times 2n$  state matrix  $A$  is

$$A = \begin{bmatrix} 0 & I \\ -\Lambda & -2\zeta\sqrt{\Lambda} \end{bmatrix} \quad (25)$$

and the  $2n \times 1$  input weighting vector  $B$  is

$$B = \begin{bmatrix} 0 \\ B_i \end{bmatrix} \quad (26)$$

**PVDF Sensor Equation** The output signal was assumed to be measured by the PVDF sensors, shown in Figure 13. The model of the charge developed on the  $k$ th piezoelectric sensor, developed by Lee and Moon[13] [14], is

$$q_k(t) = -\frac{1}{2} \int_{\Omega_k} z \left( e_{31} \frac{\partial^2 w(x, y, t)}{\partial x^2} + e_{32} \frac{\partial^2 w(x, y, t)}{\partial y^2} \right) dx dy, \quad (27)$$

where  $z = (h_p + h_s)/2$  with  $h_p$  and  $h_s$  being the thicknesses of the piezoelectric patch and of the structure respectively, and  $e_{31}$  and  $e_{32}$  are piezoelectric constants.  $\Omega_k$  represents the domain of the  $k$ th sensor, while  $w(x, y, t)$  is the displacement in the out-of-plane direction. The time dependence of  $q_k(t)$  is induced because of the time dependence of  $w(x, y, t)$ . Substituting Eq. (20) into Eq. (27), the sensor charge is

$$q_k(t) = \sum_{i=1}^n \left[ -\frac{1}{2} \int_{\Omega_k} z \left( e_{31} \frac{\partial^2 \phi_i(x, y)}{\partial x^2} + e_{32} \frac{\partial^2 \phi_i(x, y)}{\partial y^2} \right) dx dy \right] \eta_i(t) \quad (28)$$



Furthermore, since  $i(t) = dq/dt$ , the current signal due to the mechanical deformation of the structure is

$$i_k(t) = \sum_{i=1}^n \left[ -\frac{1}{2} \int_{\Omega_k} z \left( e_{31} \frac{\partial^2 \phi_i(x, y)}{\partial x^2} + e_{32} \frac{\partial^2 \phi_i(x, y)}{\partial y^2} \right) dx dy \right] \dot{\eta}_i(t) \quad (29)$$

In practice, if displacement is the measurement desired, a charge amplifier should be connected to the PVDF patches, and if the measurement desired is velocity, a current amplifier should be used.

The optimization process, described in detail in the next section, selects the sensor distribution and the control law to minimize a specified objective function. To accomplish this, the homogenization approach was used to express the piezoelectric coefficients,  $e_{31}$  and  $e_{32}$ , in terms of the optimization parameters  $a_v$ . Specifically, the PVDF material was modeled using the extended unit cell microstructure shown in Figure 14 which was described in detail in Section 5.1. Each unit cell is characterized by the square void with edge length  $a_v$ . The piezoelectric coefficients are then expressed as a function of  $a_v$  by homogenizing the cells through an asymptotic expansion, taking the limit to an infinite number of holes per unit cell. The resulting material laws, for  $e_{31}(a)$  and  $e_{32}(a_v)$  are shown in Figure 15. Note that negative values of  $a_v$  are permitted. While this seems inconsistent from the physical description of a "hole", mathematically this is quite convenient. It captures the notion of oppositely polled PVDF material by expressing the piezoelectric coefficients as

$$e_{ij}^h(a) = \text{sign}(a) e_{ij}^{h*}(|a|) \quad (30)$$

where  $a \in [-1, 1]$ , and  $e_{ij}^{h*}(|a|)$  is the function obtained from homogenization [5] valid for  $a \in [0, 1]$ .

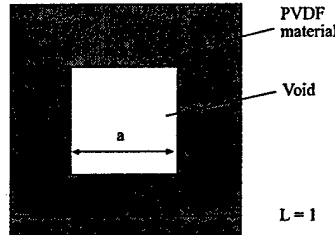
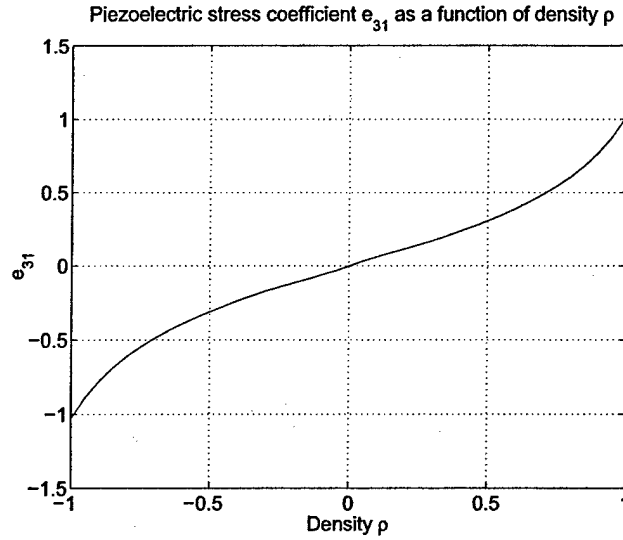


FIGURE 14: Unit cell defining the microstructure

The effect of the parameterization of the piezoelectric coefficients by  $a_v$  on the sensor equation, Eq. (28), is captured by substituting Eq. (30) into Eq. (28), yielding the new sensed charge as

$$q_k(t) = -\frac{1}{2} \int_{\Omega_k} z \left\{ e_{31}^h[a(x, y)] \frac{\partial^2 w(x, y, t)}{\partial x^2} + e_{32}^h[a(x, y)] \frac{\partial^2 w(x, y, t)}{\partial y^2} \right\} dx dy \quad (31)$$

FIGURE 15: Homogeneous  $e_{31}$  as a function of density  $\rho$  for a microstructure

The output matrix  $C$  of Eq. (24) is assembled by replacing the displacements  $w(x, y, t)$  by the assumed modes expansion of Eq. (20) yielding the output matrix components

$$C_d(k, i) = -\frac{1}{2} \int_{\Omega_k} z \left( e_{31}^h[a(x, y)] \frac{\partial^2 \phi_i(x, y)}{\partial x^2} + e_{32}^h[a(x, y)] \frac{\partial^2 \phi_i(x, y)}{\partial y^2} \right) dx dy \quad (32)$$

and thus the output matrix is

$$C = \begin{bmatrix} C_d(1, 1) & C_d(1, 2) & \dots & C_d(1, n) & 0 & 0 & \dots & 0 \\ \dots & & & & & & & \\ C_d(m, 1) & C_d(m, 2) & \dots & C_d(m, q) & 0 & 0 & \dots & 0 \\ 0 & 0 & \dots & 0 & C_d(1, 1) & C_d(1, 2) & \dots & C_d(1, n) \\ \dots & & & & & & & \\ 0 & 0 & \dots & 0 & C_d(m, 1) & C_d(m, 2) & \dots & C_d(m, q) \end{bmatrix} \quad (33)$$

For the one-dimensional beam example considered here the mode shapes  $\phi(x)$  are not functions of  $y$ , and the piezoelectric coefficient  $e_{32}^h$  is zero thus simplifying the calculation of Eq. (33).

**Control Strategy Description** In the system simulation,  $n = 20$  eigenmodes were considered, where the goal was to damp the first  $m = 5$  modes. The remaining  $n - m$  residual modes were left in the model to capture possible spillover effects. The control design, however, was based on the truncated model with only 5 modes. The truncated model will be denoted

$$\begin{aligned} \dot{\tilde{x}} &= \tilde{A}\tilde{x} + \tilde{B}u \\ \tilde{y} &= \tilde{C}\tilde{x} \end{aligned} \quad (34)$$

where  $\tilde{x}$  is a  $2m \times 1$  truncated state vector,  $\tilde{A}$  is a  $2m \times 2m$  state matrix,  $\tilde{B}$  is a  $2m \times 1$  input weighting vector,  $\tilde{C}$  is a  $2m \times 2m$  output matrix.

A state feedback controller was used where

$$u = -K^T \tilde{x} = -K^T R_d x \quad (35)$$

where  $R_d$  is  $\tilde{C}^{-1}C$ , and the  $2m \times 1$  gain vector  $K$  was obtained using the LQR method

$$K = \frac{1}{r} \tilde{B} P \quad (36)$$

The scalar control effort weighting is denoted  $r$ , and the  $2m \times 2m$  matrix  $P$  is the solution to the matrix Ricatti equation

$$\tilde{A}^T P + P \tilde{A} - \frac{1}{r} P \tilde{B} \tilde{B}^T P + Q = 0 \quad (37)$$

where the weighting matrix for the state  $Q$  was chosen as

$$Q = \begin{bmatrix} \Lambda & 0 \\ 0 & I \end{bmatrix} \quad (38)$$

Based on  $r$  and  $Q$ , the average energy (both kinetic and potential) contained in the oscillation and total energy consumed by the controller are minimized at the same time. This minimum value of  $r$  reflects the maximum feedback gain resulting in a neutrally stable system.

Although LQR is used in this study, it should be noted that in practice the required state vector is not measured directly, and thus a state estimator would need to be used [20]. This, however, does not change the main results of this work and the focus on combined sensor and control law optimization.

**Formulation of the Optimal Design Problem** Simultaneous controller and system optimization problems can be classified into one of two types, (1) Direct Gain Optimization or (2) Indirect Gain Optimization. The direct gain optimization approach assumes a postulated control strategy with some gains or parameters unspecified. A numerical optimization process is then used to select the gains of the controller and the parameters that define the structure's design to minimize some performance criteria. The indirect approach, as employed in this work, seeks to enhance the system's performance without explicitly specifying the actual gains of the controller. In this example, reducing spillover sensitivity is the main goal, for a specified controller form (LQR). Once the sensor topology is formed through the optimization process, the designer has the ability to select a wide range of possible controller gains. This method has the attractive feature of yielding a controller/system design that is more flexible as compared to the direct gain approach. In the remainder of this section the optimization problem is formulated for two different cost functions.

Each PVDF sensor, for both the discrete and the segmented distributed design domains of Figure 13, was divided into  $p$  segments. The piezoelectric properties of each segment was uniquely characterized by its density-like parameter  $a_v$ . The set of  $5p$  parameters (since there are 5 sensors), denoted  $\mathcal{A}$ , constituted the only free variables in the optimization process.

Two cost functions were considered. The first one, denoted  $\mathcal{J}_1$ , was based on the observability gramian, where the idea was to improve the system's stability margin by suppressing the observation spillover of the residual modes. The other, denoted  $\mathcal{J}_2$ , was simply the LQR control weighting scalar  $r$ .

According to Hac (1993)[11], if the natural frequencies of the structure are well spaced and the damping coefficients are small, then the system's observability gramian can be approximated as

$$W_o = \begin{bmatrix} \frac{\beta_{11}}{4\zeta_1\omega_1} & 0 & \dots & \\ 0 & \frac{\beta_{22}}{4\zeta_2\omega_2} & 0 & \dots \\ & & & 0 \\ & \dots & 0 & \frac{\beta_{qq}}{4\zeta_q\omega_q} \end{bmatrix}. \quad (39)$$

The values  $\zeta_i$  and  $\omega_i$  are the modal damping coefficients and natural frequencies of the open loop system. The quantity  $\beta_{ii}$  is defined as

$$\begin{aligned} \beta_{ii} &= 1 & \text{if } i \in 1..m \\ \beta_{ii} &= \sum_{k=1}^m R_d^2(i, k) & \text{if } i \in m+1..q \end{aligned} \quad (40)$$

Using this notation, the first cost function is defined as

$$\mathcal{J}_1(\mathcal{A}) = \left( \max_{i \in \mathcal{V}} \frac{\beta_{ii}}{\Delta \zeta_i^c \omega_i^c} \right) \left( \frac{\lambda_{\max}^{C_d}}{\lambda_{\min}^{C_d}} \right)^\eta \quad (41)$$

where  $\mathcal{V}$  is the set of modes whose observability gramian entries are to be minimized. Since the goal was to control the first  $m$  modes,  $\mathcal{V}$  should contain the modelled modes greater than  $m$ . The superscript  $c$  on  $\omega_i$  and  $\zeta_i$  indicates a closed-loop quantity.  $\lambda_{\min}^{C_d}$  and  $\lambda_{\max}^{C_d}$  are minimum and maximum eigenvalues of  $C_d$ . The term

$$\left( \frac{\lambda_{\max}^{C_d}}{\lambda_{\min}^{C_d}} \right)^\eta \quad (42)$$

denotes the damped conditioning number. This definition is computationally meaningful only provided the conditioning number of the matrix (the ratio of the largest to the smallest eigenvalue) is not larger than the inverse of the machine accuracy or relative round off error. For the smart structure application, we desire good sensing of the first  $m$  modes, which the conditioning number of  $C_d$  ensures.  $\eta$  denotes a numerical damping coefficient [23] that is selected in an ad-hoc manner to aid the optimization convergence. In this study a value of  $\eta = 1.6$  was used.

The optimization problem can be summarized as finding the parameter set  $\mathcal{A}$  that minimizes Eq. (41) whose terms  $\beta_{ii}$ ,  $\zeta_i^c$ , and  $\omega_i^c$  are the result of implementing an LQR controller, designed from the  $m$  mode truncated model of Eq. (34), on the  $n$  mode design model of Eq. (24). Each design parameter of  $\mathcal{A}$  is constrained such that  $0 \leq a_i \leq 1$ .

The second cost function is the LQR control weighting term, or,

$$\mathcal{J}_2(a) = \min(r) \quad (43)$$

with the constraint that all closed-loop poles  $p_i^c$  have the property that

$$\text{Re}(p_i^c) \leq 0 \quad (44)$$

This ensures the system is stable. Small values of the cost function  $\mathcal{J}_2(a)$  mean that large values of the overall closed-loop gain can be permitted without causing instability.

Similar to the previous cost function, the optimization problem can be summarized as finding the parameter set  $\mathcal{A}$  that minimizes Eq. (43) such that the closed-loop poles of the  $n$  mode design model of Eq. (24) are stable where its LQR controller is designed based on the  $m$  mode truncated model of Eq. (34). Again, each design parameter of  $\mathcal{A}$  is constrained such that  $0 \leq a_i \leq 1$ .

A sequential quadratic programming, numerical optimization code was used to solve both optimization problems where the initial values of all the design parameters were set to 1.0. Due to the complexity of the problem, no proof was found to indicate a globally optimal solution. From a design perspective, this is acceptable since the optimization process does provide a better design than using the nominal, full-density sensor distribution. Finally, since the pinned-pinned beam mode shapes are symmetric about the geometric center, A half-beam optimization approach was used, thus reducing the number of optimizeable parameters by one half.

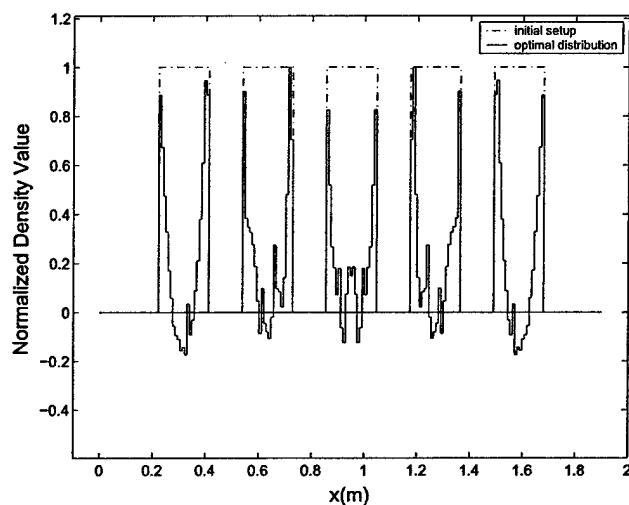
	Initial Distribution	$\mathcal{J}_1^*$ Distribution	$\mathcal{J}_2^*$ Distribution
$\mathcal{J}_1$	121.68	0.9368	116.8091
$\mathcal{J}_2$	0.0594	0.0103	0.00385

TABLE 2: Cost Function Values of Optimal Distribution of Discrete PVDF

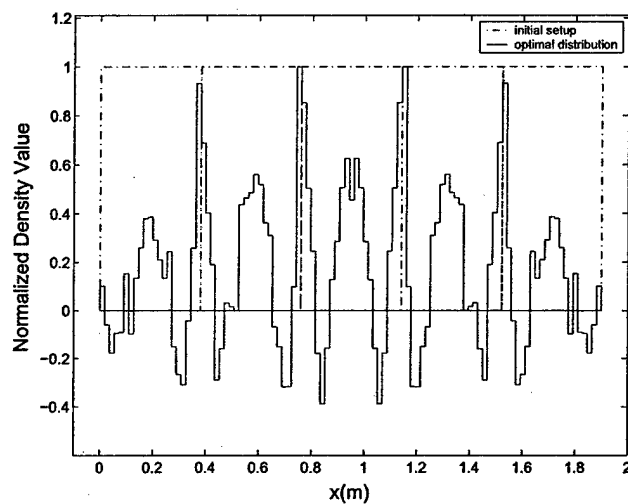
	Initial Distribution	$\mathcal{J}_1^*$ Distribution	$\mathcal{J}_2^*$ Distribution
$\mathcal{J}_1$	3.0524	0.0468	0.6887
$\mathcal{J}_2$	0.0267	0.00073	0.000249

TABLE 3: Cost Function Values of Optimal Distribution of Segmented Distributed PVDF

**Optimal Sensor and Controller Design Results** For each sensor configuration the sensor density and control law were optimized simultaneously for the two cost functions described in the previous section. Table 2 summarizes the results for the discrete sensor case, and Table 3 shows the results for the segmented, distributed case. In addition to showing the change in cost from the initial densities ( $\rho_v = 1$ ) to the optimal, the non optimized cost function is evaluated. For example, the first row of Table 2 shows the initial value of  $\mathcal{J}_1$ , the value of  $\mathcal{J}_1^*$  (where \* denotes an optimal quantity) and finally the value of  $\mathcal{J}_1$  using the distribution that produced  $\mathcal{J}_2^*$ . This helps to illustrate the differences between cost functions.

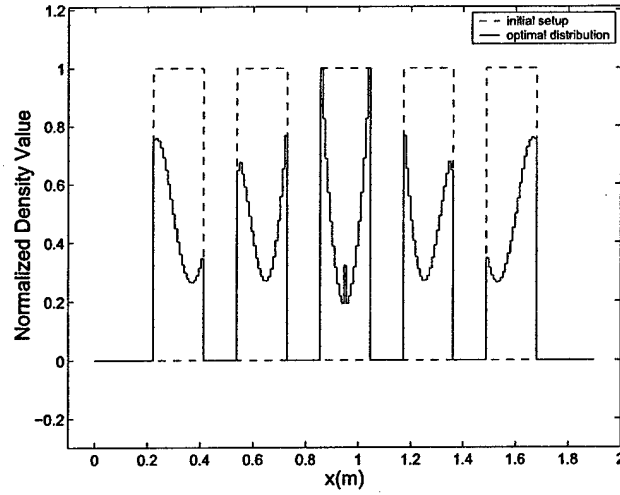


(A) Beam with the discrete PVDF sensor configuration ( $\mathcal{J}_1=0.9368$ )

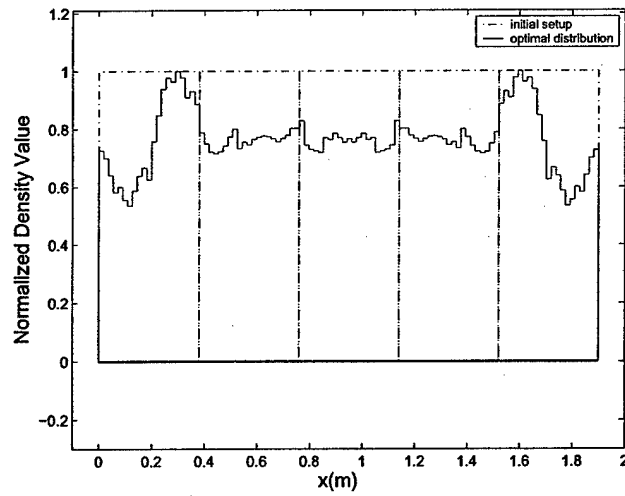


(B) Beam with segmented, distributed PVDF sensor configuration ( $\mathcal{J}_1=0.468$ )

FIGURE 16: The optimal normalized PVDF density as a function of beam position for both sensor configurations. In both cases the PVDF was optimized using the observability gramian cost function  $\mathcal{J}_1$ .

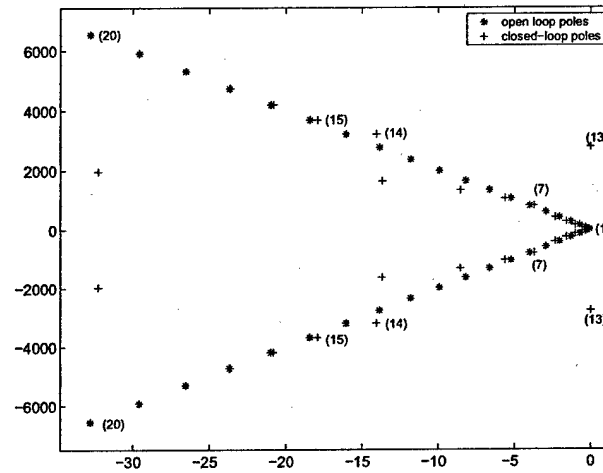


(A) Beam with the discrete PVDF sensor configuration  
( $\mathcal{J}_2=0.00385$ )

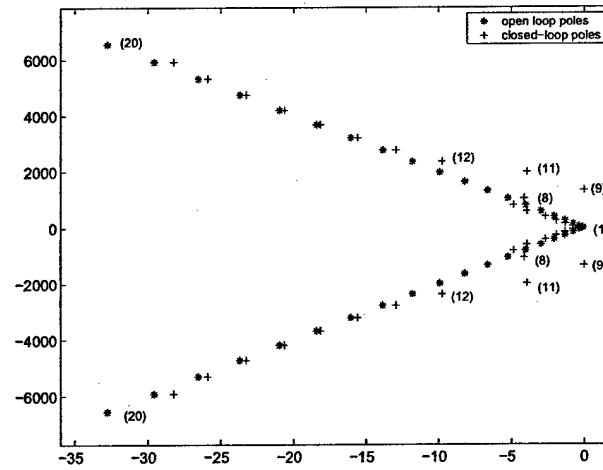


(B) Beam with segmented, distributed PVDF sensor  
configuration ( $\mathcal{J}_2=0.000249$ )

FIGURE 17: The optimal normalized PVDF density as a function of beam position for both sensor configurations. In both cases the PVDF was optimized using the LQR stability margin cost function  $\mathcal{J}_2$ .



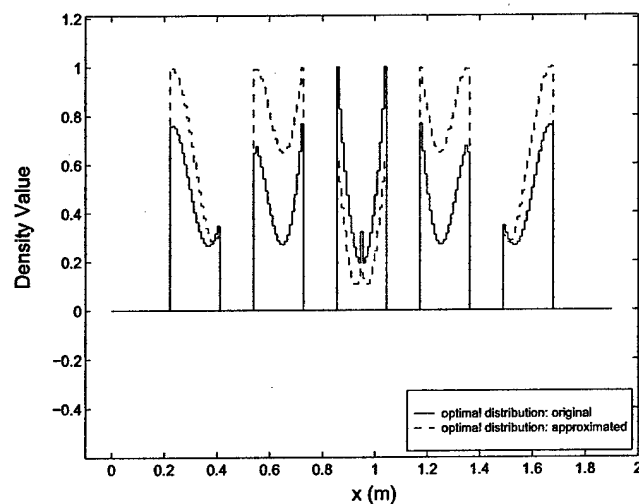
(A) Beam with the discrete PVDF sensor configuration



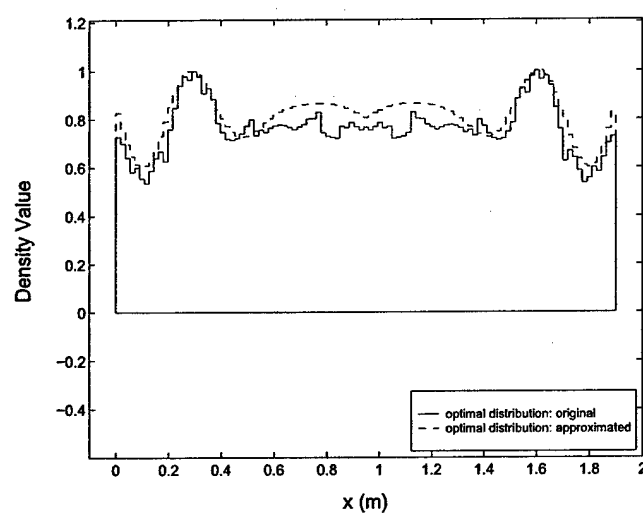
(B) Beam with the segmented, distributed PVDF sensor configuration

FIGURE 18: Pole locations with uniform density distributions. Mode numbers are given for select mode shapes.





(A) Beam with the approximate discrete PVDF sensor configuration ( $\mathcal{J}_2=0.0046$ )



(B) Beam with the approximate segmented, distributed PVDF sensor configuration ( $\mathcal{J}_2=0.000965$ )

FIGURE 19: The approximate optimal normalized PVDF density for both sensor configurations.

Mode Number	Observability Gramian Values					
	Initial		$\mathcal{J}_1$ Optimal		$\mathcal{J}_2$ Optimal	
	Disc.	Seg. Dist.	Disc.	Seg. Dist.	Disc.	Seg. Dist.
6	0	0.1908	0.0129	0.0464	0.0949	0.1275
7	0.1939	0.3392	0.2862	0.0457	1.8330	0.3320
8	0.4995	0.7631	0.0033	0.0010	0.0053	0.0027
9	1.6053	3.0524	0.8714	0.0350	1.5881	0.5292
10	7.9914	0	0.9160	0.0275	9.8149	0.4927
11	121.6804	3.0524	0.9368	0.0430	116.8091	0.6887
12	0	0.7631	0.9614	0.0468	1.5047	0.3930
13	99.0245	0.3392	0.9614	0.0466	8.1072	0.2689
14	5.2304	0.1908	4.2907	0.4026	1.0705	0.2266
15	0.8228	0.1221	22.7815	1.5989	14.7049	0.3220
16	0.1908	0.1908	4.0236	5.7998	2.0425	0.4112
17	0.0503	0.3392	3.4876	50.2938	2.2847	1.5027
18	0	0.7631	0.1794	75.7091	1.5628	1.1079
19	0.006	3.0524	1.8262	922.4670	11.1493	1.5256
20	0	0	7.1655	1.1942	0.3801	0.0331

TABLE 4: Comparison of observability gramian values for both sensor domains ('Disc' = Discrete, 'Seg. Dist' = Segmented Distributed). In addition to the nominal distributions, both the  $\mathcal{J}_1$  and  $\mathcal{J}_2$  optimal distributions are shown.

**Discussion** When considering the lower values of Table 3 it appears that regardless of the cost function used, the segmented, distributed sensor configuration yields better results than that of the discrete sensor. The only caveat to this conclusion is illustrated in the 4th column of Table 4 which shows the observability gramians for each uncontrolled mode of the simulation. Specifically, when the segmented, distributed sensor is used with the observability gramian cost function,  $\mathcal{J}_1$ , residual modes 17-19 acquire a large, and potentially poor, observability gramian value. It should be noted that in the last column of Table 4 does not show the opposite effect. That is, when the distribution is optimized with respect to the LQR stability margin the observability gramian values do not have any extreme values. These features suggest that the segmented distributed sensor configuration, along with LQR stability margin optimization,  $\mathcal{J}_2$ , is the best choice.

This conclusion is further justified when considering the smoothness of the actual PVDF density profiles of Figure 16 and Figure 17. Specifically, fabrication of variable density active material is a rather new discipline with limitations on gradients. In all cases the LQR stability margin optimal distributions were smoother than the observability gramian ones. This is especially true for the segmented distributed configuration of Figure 17(b) where the density profile may be approximated by a simple trapezoidal shape.

It can be seen in Figure 16 and Figure 17 that sensor density distribution depends on what cost function is used. The  $r_{min}$  optimal distribution of Figure 17 has all positive densities. This can be interpreted as all sensors being on one side of the beam. This is an important result, because it implies that better performance of the structure is achieved

when sensors are distributed uni-sided. Practically, it could imply simpler manufacturing and more cost-effective active structures.

The shape of the distribution also has some physical significance. To illustrate this, we will focus on the  $r_{min}$  optimal cases of Figure 17. The goal of the  $r_{min}$  optimization is to find the parameter set  $\mathcal{A}$  that allows for the largest LQR gains while still maintaining stability. Increasing the gains beyond this point results in closed-loop poles migrating to the right half of the complex plane. The shape of the optimal distribution is related to the mode shapes of the poles that are the first to go unstable. To illustrate this, plots were constructed that show the open loop and closed-loop poles for both the discrete and segmented distributed sensor configurations, shown in Figure 18. For the discrete sensor case of Figure 18(a), modes 7, 13, 14, and 15 are most likely to go unstable as the loop gain is increased. For the segmented distributed case of Figure 18(b), modes 8, 9, 11 and 12 go unstable. The density distributions of Figure 17(a) and Figure 17(b) are strongly influenced by these mode shapes. More specifically, approximate optimal solution can be constructed, and are shown in Figure 19, where the distributions are formed as linear combinations of these mode shapes. The equations used to generate the approximate densities of Figure 19 are

$$\rho_a = 3 + \phi_7 - 0.3\phi_{13} - \phi_{14} + \phi_{15} \quad (45)$$

$$\rho_b = 10 - 0.5\phi_8 - \phi_9 - \phi_{11} - 0.3\phi_{12} \quad (46)$$

where the mode shape  $\phi_i$  are denoted in Eq. 21, and the suboptimal  $r_{min}$  cost functions are 0.0046 and 0.000965 for the densities of Figure 17(a) and Figure 17(b) respectively. This compares favorably to the optimal costs of 0.00385 and 0.000249. To summarize, the shape of the optimal distributions allow the controller to better sense those modes that contribute the most to limiting the stability margin.

### 5.3.2 Simultaneous Optimization of an Active Structure

The main objective of this research is to develop and assess a method for simultaneous optimization of active structures considering the conventional structure topology, active material layout, and the control system. In this section this method is used to demonstrate the robust control of a piezoelectric laminate beam by simultaneously optimizing the conventional material distribution, active material distribution and the control system for a closed-loop system. The parallel genetic algorithm based active structure design code was used, including ABAQUS for model development and Matlab® for control design. The structure was initialized as a grid of cells with complete structural and energetic properties. During the optimization process, structural material and active material was removed from the cells to minimize a multi-objective cost function. In order to demonstrate the improvement of the control efficiency, the optimally designed system was compared to a conventional design consisting of a cantilever alluminum beam with a PZT patch actuator at the root and 2 PVDF sensors fully covering the beam's underside.

**Dynamics of a Piezoelectric Laminate Beam** The cantilever flexible structure with one PZT actuator and two PVDF sensors as shown in Figure 20 was considered. The physical dimensions for the beam are given in Table 5.

	Parameter	Units	Value
beam	$L_b$	$m$	0.32
	$w_b$	$m$	0.03
	$t_b$	$m$	0.001
	$\rho$	$kg/m^3$	2700
	$E$	$N/m^2$	$69 \times 10^9$
PZT	$L_a$	$m$	0.8
	$w_a$	$m$	0.03
	$t_a$	$m$	$0.267 \times 10^{-3}$
	$x_1$	$m$	0
	$x_2$	$m$	0.08
	$e_{31a}^0$	$m/V$	12.54
	$e_{32a}^0$	$m/V$	12.54
PVDF	$L_s$	$m$	0.32
	$w_s$	$m$	0.019
	$t_s$	$m$	$9 \times 10^{-6}$
	$e_{31s}^0$	$m/V$	0.046
	$e_{32s}^0$	$m/V$	0.046

TABLE 5: Physical parameters of the cantilever beam of the example.

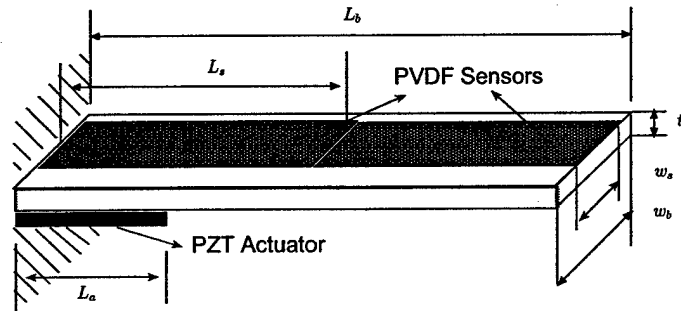


FIGURE 20: Cantilever beam model.

The beam's transverse deflection at point  $x$  and time  $t$  is denoted  $w(x, t)$ , assuming the beam as a one-dimensional system only. The partial differential equation (PDE) which describes the dynamics of the beam is

$$EI \frac{\partial^4 w(x, t)}{\partial x^4} + \rho A \frac{\partial^2 w(x, t)}{\partial t^2} = \frac{\partial^2 M_a(x, t)}{\partial x^2} \quad (47)$$

where  $\rho$ ,  $A$ ,  $E$ , and  $I$  represent density, cross-sectional area, Young's modulus of elasticity, and moment of inertia about the neutral axis of the beam, respectively.

The general equation of motion can be described as

$$\ddot{\eta}_i(t) + 2\zeta\sqrt{\Lambda}\dot{\eta}_i(t) + \Lambda\eta_i(t) = B_i V_a(t) \quad (48)$$

where  $\zeta$  are the modal damping coefficients,  $\Lambda$  is the matrix of eigenvalues and the control weighting coefficient of the  $i$ th mode,  $B_i$ , is

$$B_i = -\frac{1}{2} \int_{\Omega} z_2 \left( e_{31a} \frac{\partial^2 \phi_i(x, y)}{\partial x^2} + e_{32a} \frac{\partial^2 \phi_i(x, y)}{\partial y^2} \right) dx dy \quad (49)$$

where  $\Omega$  is the actuator domain. Using the homogenization approach to map cell densities to material properties and Eq. (28), the sensor equation and the actuator equation in response to density can be obtained

$$C_a(k, i) = -\frac{1}{2} \int_{\Omega_k} z_1 \left( e_{31s}^h [\rho_v(x, y)] \frac{\partial^2 \phi_i(x, y)}{\partial x^2} + e_{32s}^h [\rho_v(x, y)] \frac{\partial^2 \phi_i(x, y)}{\partial y^2} \right) dx dy \quad (50)$$

$$B_i = -\frac{1}{2} \int_{\Omega} z_2 \left( e_{31a}^h [\rho_v(x, y)] \frac{\partial^2 \phi_i(x, y)}{\partial x^2} + e_{32a}^h [\rho_v(x, y)] \frac{\partial^2 \phi_i(x, y)}{\partial y^2} \right) dx dy \quad (51)$$

The objective of the experiment was to increase the stability margin of the closed-loop system and control the beam's first two modes of vibration using an LQR control law with the cost function of Eq. 43. A block diagram of the closed-loop system is shown in Figure 21. Densities of the PVDF sensor, the PZT actuator and the beam were considered optimizeable

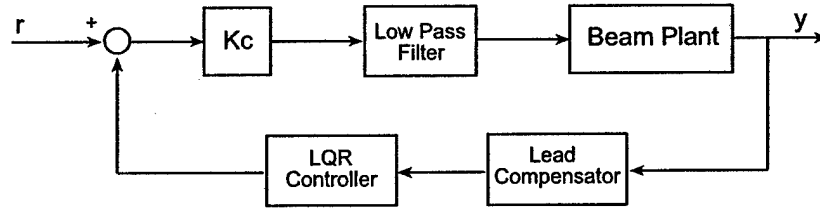


FIGURE 21: Control block diagram.

parameters of the cost function  $R_{min}$  which provides a wide range of possible gains to ensure the system is stable. Simply, with optimal density distributions, the designer has the ability to select a larger gain in comparison to that of a nominal, uniform density design.

**Simulation and Experimental Results** The plant model used during optimization captures the first 3 modes of the beam. Since the control objective focuses on only the first two modes, the third mode is included so that the final design is more resilient to third mode spillover. To illustrate the spillover effect for the nominal, uniform density beam, its closed-loop pole locations are shown in Figure 22. From this figure it is evident that the system will eventually become unstable as the feedback gain increases.

Before beginning the optimization process it is important that the model be predictive of the physical system. To gauge this, the nominal beam with PVDF sensors was tested and compared to a simulation of the 3 mode model. The resulting comparison of this open-loop case is shown in Figure 23.

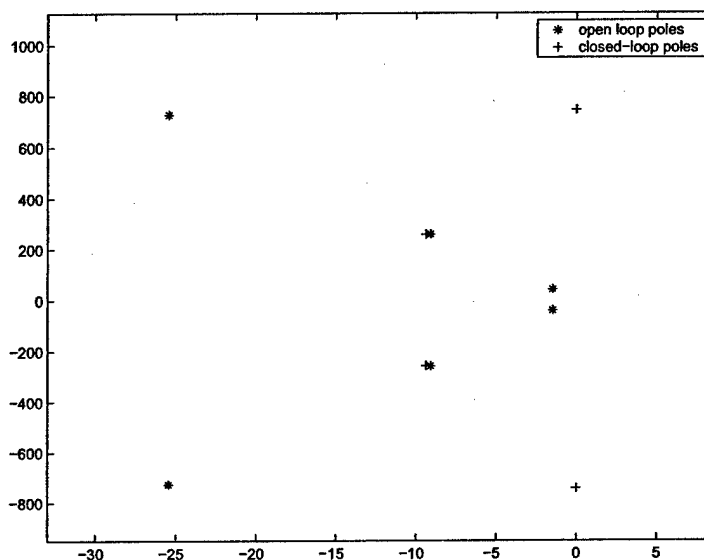
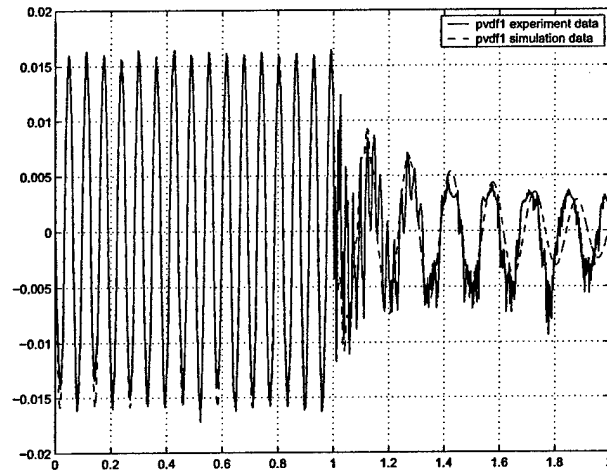


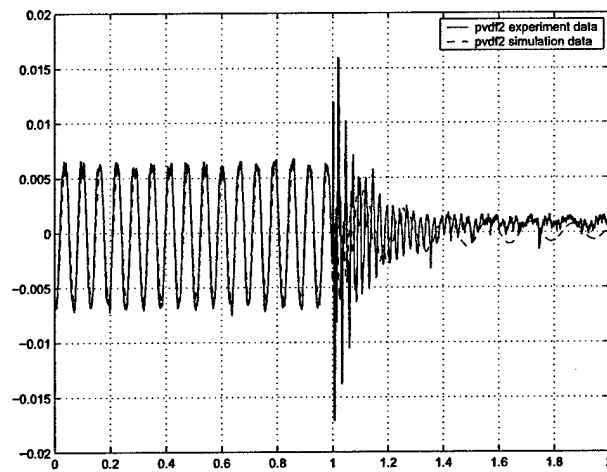
FIGURE 22: Pole locations of the system with initial density setup.

The objective of the optimization process was to find a design defined by the density distributions of the conventional beam, PZT actuator, and PVDF sensors yielding a larger stability margin than the nominal uniform density case. The design environment described earlier, consisting of a parallel processing Genetic Algorithm optimization engine, ABAQUS for model generation, and Matlab<sup>®</sup> for control design, was used with 20000 members in the initial population. 20 population generations were created where the simultaneous design code ran on 20 workstations in parallel. The "raw" optimal solution is shown in Figure 24(a), and yielded an  $r_{min}$  of 0.004 as compared to  $r_{min} = 0.3165$  for the nominal beam with completely covered PVDF and PZT material. Since the discontinuous distributions would be difficult to machine, smoothed distributions were generated using a 6th order polynomial fit to the optimal distributions, similar to the approach used in Section 5.3.1. This changed the cost only slightly, increasing  $r_{min}$  to 0.0041. These are plotted in Figure 24(b). It should be noted that the widths of the various materials were constrained according to: PZT material  $> 0.5$ , PVDF material  $> 0.5$  and the conventional material  $> 0.65$ .

Figure 25 shows time histories of the nominal closed-loop system to the optimal closed-loop system. Since the  $r_{min}$  was decreased by a factor of 80 for the optimal system, the loop

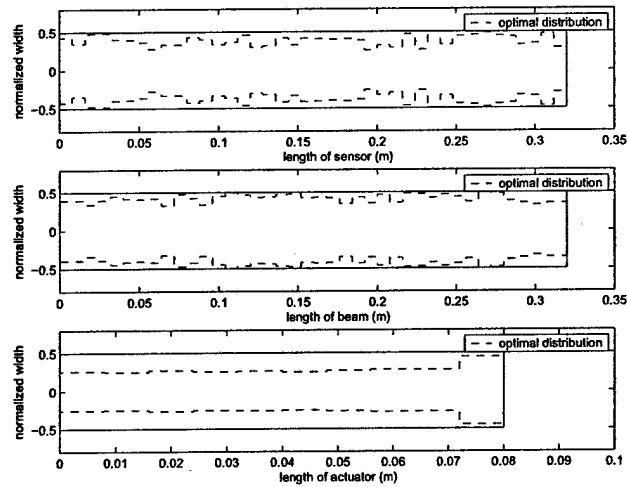


(A) Signals of the 1st PVDF sensor

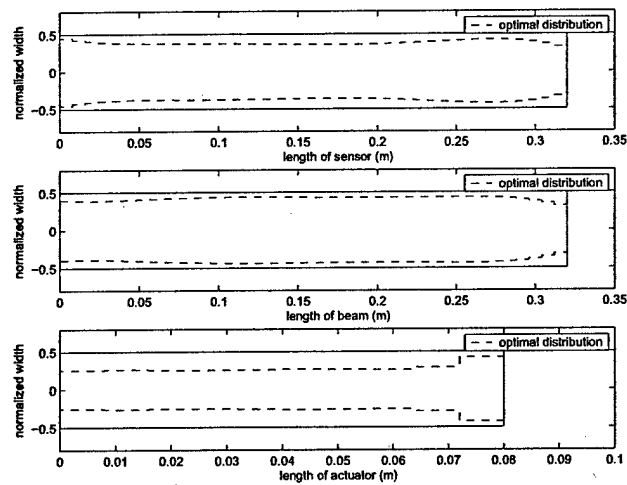


(B) Signals of the 2nd PVDF sensor

FIGURE 23: Simulation and Experiment sensor signals of the open loop system.



(A) Optimal distributions using GA method

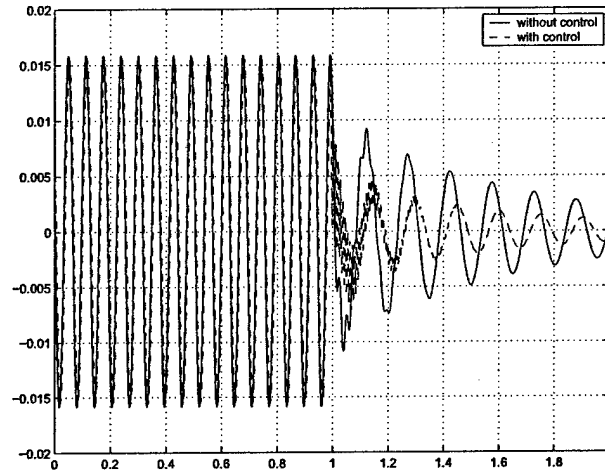


(B) Smooth optimal distributions after interpolated

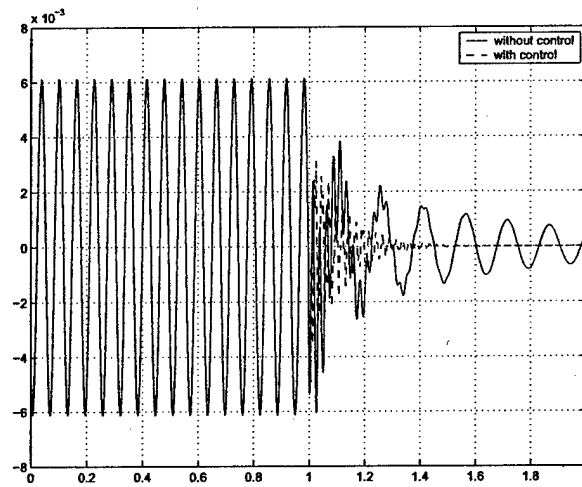
FIGURE 24: Optimal distributions for conventional beam, PZT actuator and PVDF sensor.



gain could be increased as compared to the nominal system while still ensuring closed-loop stability. This resulted in a minimum decrease in strain by a factor of 1/2 as can be seen in Figure 25



(A) Signals of the 1st PVDF sensor



(B) Signals of the 2nd PVDF sensor

FIGURE 25: Simulated sensor signals of the optimal, closed-loop system.

## 6 Publications

The publications listed below are divided into those in archival journals, conference proceedings, and theses.

### 6.1 Peer-Reviewed Publications

1. Buehler, M. J., Bettig, B. P., and Parker, G. G., 2003, 'Numerical Homogenization of Smart Material Finite Element Cells,' *Communications on Numerical Methods in Engineering*, Accepted for Publication.
2. Chen, W., Buehler, M., Parker, G. G., and Bettig, B., 2003, 'Optimal Sensor Design and Control of Piezoelectric Laminate Beams,' *IEEE Transactions on Control System Technology*, Accepted for Publication.
3. Buehler, M. J., Bettig, B. P., and Parker, G. G., 2003, 'Topology Optimization of Smart Structures using a Homogenization Approach', *Journal of Intelligent Material Systems and Structures*, Accepted for Publication.

### 6.2 Publications in Conference Proceedings

1. Chen, W., Buehler, M., Parker, G. G., and Bettig, B., 2003, 'Robust Design and Control of Piezoelectric Laminate Beams Using a Simultaneous Optimization Method,' *SPIE 10th Annual International Symposium on Smart Structures and Materials*, March 3-6.
2. Buehler, M., Bettig, B., and Parker, G. G., 2002, 'Topological Optimization of Smart Structures Using an Homogenization Approach,' *SPIE 9th Annual International Symposium on Smart Structures and Materials*, San Diego CA, March 18-20.

### 6.3 Theses

1. Buehler, M., 2001, 'Homogenization of Smart Material Cells for Topological Optimization,' Master's Thesis, Michigan Technological University.

## 7 Interactions and Transitions

Professors Parker and Bettig have communicated the capabilities of the Parallel Genetic Algorithm Active Structure Design Code to contacts at AFRL/MNAV. We are currently exploring their interest in using it for cruise missile active wing twist design. This would require some new development in the area of implementing aerodynamic load models into the existing finite element portion of the code.

Another notable interaction has developed through one of the M.S. students working on the project. Specifically, Markus Buehler received his M.S. degree from Michigan Technological University in 2001, and then went to the Max-Planck Institute in Germany. He is still an active participant in the project, and has facilitated important technical relationships between Michigan Tech and the Max-Planck Institute.

## 8 New Discoveries, Inventions, and Patent Disclosures

The project resulted in the creation of the Parallel Genetic Algorithm Active Structure Design Code described in detail in the Accomplishment section of the report. Since it relies on a general, off-the-shelf structural analysis code (ABAQUS) and an equally powerful control design tool (Matlab<sup>®</sup>), its applicability is broad and covers most active structure design possibilities.

## 9 Honors and Awards

- G. Parker was promoted to the rank of Associate Professor in 2001.
- G. Parker received the Michigan Technological University Distinguished Teaching Award in 2001.
- G. Parker received the Society of Automotive Engineers Ralph E. Teetor Award in 2002.

## References

- [1] M. J. Balas. Active control of flexible systems. *Journal of Optimization Theory and Application*, 25(3), 1978.
- [2] K.-J. Bathe. *Finite Element Procedures in Engineering Analysis*. Prentice-Hall, Inc., 1982.
- [3] M.P. Bendsøe. Optimal shape design as a material distribution problem. *Structural Optimization*, 1:193–202, 1989.
- [4] A. Bensoussan, J.L. Lions, and G. Papanicolaou. *Asymptotic Analysis for Periodic Structures*. ISBN 0-444-85172-0. North Holland Publishing Company, 1978.
- [5] M. J. Buehler, B. P. Bettig, and G. G. Parker. Topological optimization of smart structures using an homogenization approach. In *Proceedings of the 9th Annual International Symposium on Smart Structures and Materials*, pages 148–160, March 2002.
- [6] M.J. Buehler, B. Bettig, and G. Parker. Numerical homogenization of smart material finite element cells. *Accepted for publication in: Communications in Numerical Methods in Engineering*, 2003.
- [7] J.B. Burl. *Linear Optimal Control:  $H_2$  and  $H_\infty$  methods*. ISBN 0-201-80868-4. Addison Wesley Longman, Inc., 1999.
- [8] B.C. Chen, E.C.N. Silva, and N. Kikuchi. Advances in computational design and optimization with application to mems. *International Journal for Numerical Methods in Engineering*, 52:23–62, 2001.
- [9] M. Collet. Shape optimization of piezoelectric sensors dealing with spill-over instability. *IEEE Transactions on Control Systems Technology*, 9(4):654–662, July 2001.
- [10] J. Francu. Homogenization of linear elasticity equations. *Aplikace Matematiky, Oslo*, 27:96–117, 1982.
- [11] A. Hac and L. Liu. Sensor and actuator location in motion control of flexible structures. *Journal of Sound and Vibration*, 167(2):239–261, 1993.
- [12] N. Kikuchi and M.P. Bendsøe. Generating optimal topologies in structural design using a homogenization method. *Computer Methods Appl. Mech. Engrg.*, 71(2):197–224, 1988.
- [13] C. K. Lee. Theory of laminated piezoelectric plates for the design of distributed sensors/actuators. part 1: Governing equations and reciprocal relationships. *Journal of the Acoustical Society of American*, 87(3):1144–1158, 1990.
- [14] C. K. Lee and F. C. Moon. Laminated piezopolymer plates for torsion and bending sensors and actuators. *Journal of the Acoustical Society of American*, 85(6):2432–2439, 1989.

- [15] K. B. Lim. Method for optimal actuator and sensor placement for large flexible structures. *Journal of Guidance, Control, and Dynamics*, 15(1):49–57, 1992.
- [16] G.A. Maugin and N. Turbe. Homogenization of piezoelectric composites via bloch expansions. *International Journal of Applied Electromagnetics in Materials*, 44(2):135–140, 1991.
- [17] L. Meirovitch. *Dynamics and Control of Structures*. New York: Wiley, 1990.
- [18] H.P. Mlejnek and R. Schirrmacher. An engineer's approach to optimal material distribution and shape finding. *Comp. Meth. in Appl. Mech. and Engrg.*, 106:1–26, 1993.
- [19] S. Nishiwaki, M.I. Frecker, S. Min, and N. Kikuchi. Topology optimization of compliant mechanisms using the homogenization method. *Int. J. for Numerical Methods in Engrgr.*, 42:535–559, 1998.
- [20] S. Sana and V. S. Rao. Robust control of input limited smart structural systems. *IEEE Transaction on Control Systems Technology*, 9(1):60–68, January 2001.
- [21] O. Sigmund. On the design of compliant mechanisms using topology optimization. *Mechanics of Structures and Machines*, 25(4):495–526, 1997.
- [22] O. Sigmund. A 99 line topology optimization code written in Matlab. *Struct. Multidiscpl. Optimization*, 21(2):120–127, 2000.
- [23] O. Sigmund and S. Torquato. Design of smart composite materials using topology optimization. *Smart Material Structures*, 8:365–379, 1999.
- [24] E.C.N. Silva, J.S.O. Fonseca, F.M. de Espinosa, A.T. Crumm, J.W. Halloran G.A. Brady, and N. Kikuchi. Design of piezocomposite materials and piezoelectric transducers using topology optimization - part I. *Archives of Computational Methods in Engrg*, 6:117–182, 1999.
- [25] E.C.N. Silva, S. Nishiwaki, and N. Kikuchi. Topology optimization design of flex-tensional actuators. *IEEE Transactions on Ultrasonics, Ferroelectrics, and Frequency Control*, 47(3):657–671, 2000.